*National Technical University of Athens*
*School of Rural and Surveying Engineering*
*Department of Topography*
*Laboratory of Remote Sensing*

# Probing the potential of conventional computer vision operators for the detection of meteor craters on a Martian digital terrain model

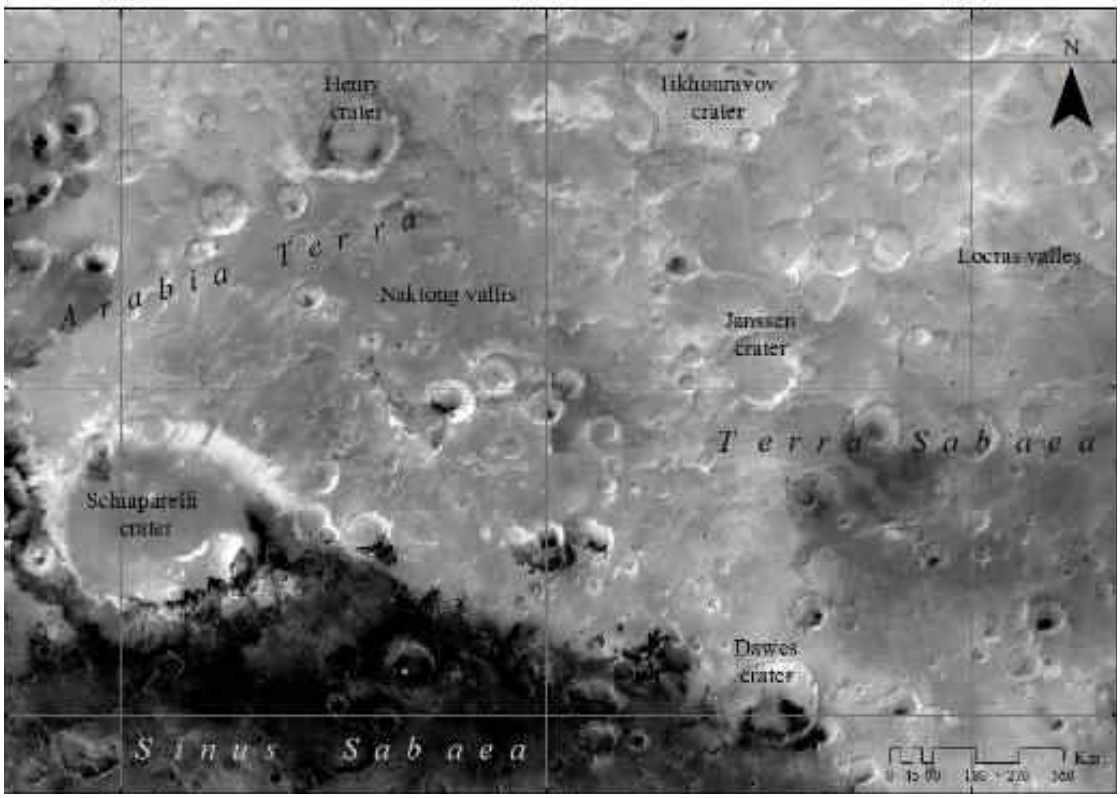


Konstantinos Athanasas, BSc (UoA), MPhil (UWA), PhD (UoA)

Supervisor: Prof. Demetre Argialas, NTUA

*Thesis submitted in partial fulfillment of the requirements for the M.Sc. Degree of Geoinformatics, School of Rural and Surveying Engineering, National Technical University of Athens NTUA.*

March 2016

**Acknowledgments**

I would like to express my gratitude to my supervisor, Prof. D. Argialas, for inspiration and guidance throughout my studies in Geoinformatics and Remote Sensing. I am especially thankful to Dr. P. Kolokoussis for the countless hours he devoted to assist me in setting the algorithms running in Python. I am also thankful to Prof. M.G. Sakellariou (SRSE, NTUA) and Prof. K. Karantzalos (SRSE, NTUA), examiners, for their valuable input. I appreciate also input from A. Argyridis, M. Dekavala and Ch. Tavlaki, PhD candidates at the Remote Sensing Laboratory, NTUA.

Konstantinos Athanasas,

Athens, 22 March 2016

**Abstract:**

This study explores the performance of two different computer-vision approaches, namely the *circular Hough transform* (CHT) and the *determinant of Hessian* (DoH), to crater detection on a digital terrain model of planet Mars. CHT exploits the edges of circular features such as craters, revealed after several steps of image processing. However, the performance of the standard version of CHT on the Martian digital terrain model generated poor results as the interference of noise from irrelevant features persistent in the processed DTM generated numerous false responses. On the other hand, published adaptations of CHT engaging additional labor to isolate much of the influence of noise were deemed as impractical for routine crater detection.

As a substitute, DoH was successful in detecting the overwhelming majority of the craters appearing on a horizontal Martian terrain. The percentage of success deteriorated as topographically more complex surfaces were encompassed. Even though, DoH scored higher than CHT despite the perplexity because DoH proved to be less sensitive to the noise than CHT. Current results, although not optimal, encourage future research to improving the performance of DoH for routine crater detection undertakings.

**Keywords**: impact craters; circular Hough transform; determinant of Hessian; space-scale

# Διερεύνηση της δυνατότητας τελεστών τεχνητής όρασης για την ανίχνευση μετεωρητικών κρατήρων σε ψηφιακό μοντέλο εδάφους του πλανήτη Άρη

Κωνσταντίνος Αθανασάς
Σχολή Αγρονόμων και Τοπογράφων Μηχανικών ΕΜΠ
Διπλωματική Εργασία Υποβληθείσα στο ΔΠΜΣ "Γεωπληροφορική"
2016

## Περίληψη

Η καταμέτρηση μετεωρητικών κρατήρων στην επιφάνεια των βραχωδών πλανητών και των δορυφόρων του ηλιακού συστήματος είναι ένας ουσιαστικός τρόπος σχετικής γεωχρονολόγησης του ανώτερου πλανητικού φλοιού (Hartman et al., 2001; Carr et al., 2010) καθώς επίσης και τρόπος μελέτης παρελθόντων παροξυσμικών φάσεων μετεωρητικών κατακρημνίσεων κατά το πρώιμο ηλιακό σύστημα (Gomes et al., 2005).

Πλήθος διαστημικών αποστολών χαρτογράφησης και τηλεπισκόπησης της επιφάνειας του πλανήτη Άρη (Pyle, 2012) κατά τη διάρκεια των τελευταίων δεκαετιών, έχουν συλλέξει δεδομένα για ολόκληρη την επιφάνεια του πλανήτη, επιτρέποντας τους πλανητικούς γεωλόγους να διεξάγουν μορφομετρικές μελέτες των μετεωρητικών κρατήρων στην επιφάνεια του Άρη (Brunetti et al., 2014). Ωστόσο, η καταμέτρηση των πολυάριθμων μετεωρητικών κρατήρων είναι μια χρονοβόρα διαδικασία.

Συχνά η γεωλογία, συνεπώς και η αστρογεωλογία, καταπιάνεται με ζητήματα που αφορούν στην ανασύνθεση του αρχικού σχήματος των γεωμορφών από τα σημερινά τους υπολείμματα, και ως εκ τούτου, συχνά τα μορφολογικά προβλήματα μπορούν να ειδωθούν ως γεωμετρικά προβλήματα (Bayer, 1985). Τέτοια προβλήματα μπορούν να αντιμετωπιστούν με τη χρήση αλγορίθμων εφαρμόσιμων σε ψηφιακά μοντέλα εδάφους (ΨΜΕ). Συνεπώς, η αναγνώριση κρατήρων διαμέσου τεχνικών τεχνητής όρασης (computer vision) είναι εξαιρετικά πρακτική στην αστρογεωλογία, καθώς μπορεί να αυτοματοποιήσει, και άρα να επιταχύνει, τη διαδικασία καταμέτρησης των κρατήρων.

Ωστόσο, οι αποσαθρωτικές και διαβρωτικές διεργασίες που λαμβάνουν χώρα στην επιφάνεια ορισμένων πλανητών (Berman et al., 2009) πιθανώς να εισάγουν τυχαίες και μόνιμες αλλοιώσεις (θόρυβος) στην αρχική μορφή (σήμα) κατά τη διάρκεια του γεωλογικού χρόνου. Αυτό ακριβώς συμβαίνει και με τους αρειανούς κρατήρες, οι ακμές των οποίων έχουν υποστεί διάβρωση από τον πάλαι ποτέ αρειανό υδρολογικό κύκλο (Andrews-Hanna et al., 2007).

Η μέθοδος Circular Hough transform (CHT) έχει προταθεί ως μέθοδος αυτόματης ανίχνευσης κρατήρων (Kim et al. 2005; Stepinski et al., 2006; Bue and Stepinski, 2007). Η μέθοδος CHT (Illingworth and Kittler, 1987) έχει θεωρητικά τη δυνατότητα να ανασυνθέσει την περίμετρο των κρατήρων, ακόμα και αν αυτοί σήμερα εμφανίζονται ατελείς λόγω διάβρωσης. Αυτό επιτυγχάνεται μεσώ μιας διαδικασίας *ψηφοφορίας* από το δισδιάστατο χώρο μιας εικόνας σε έναν δισδιάστατο ή τριασδιάστατο παραμετρικό χώρο.

Η σημερινή κατάσταση των μετεωρητικών κρατήρων μπορεί να είναι «θορυβώδης» επειδή η διάβρωση ίσως να έχει αλλοιώσει τις ακμές τους κατά τη διάρκεια του γεωλογικού χρόνου. Συνεπώς, οι πραγματικές ακμές ενός έντονα διαβρωμένου κρατήρα θα αναμένονται με κάποια πιθανότητα γύρω από το κέντρο.

Ένας άλλος τρόπος να παρακαμθεί το πρόβλημα των ατελών μορφών κρατήρων (το οποίο μπορεί να καταστήσει αναποτελεσματικές τις μεθόδους ανίχνευσης ακμών), είναι η ανίχνευση αντικειμένων θεωρώντας ότι αυτά αντιπροσωπεύουν μια ομοιογενή περιοχή στην εικόνα (blob), λαμβάνοντας υπόψη την περιοχή που αυτά καλύπτουν. Η ανίχνευση των blobs αποσκοπεί στον εντοπισμό περιοχών που εμφανίζουν τοπικά μέγιστα ή ελάχιστα. Μεταξύ των διάφορων υπολογιστικών μεθόδων αυτόματης αναγνώρισης blobs, η πιο διαδεδομένη μέθοδος (Lindeberg, 1993, 1998) είναι η *ορίζουσα του Εσσιανού πίνακα* (determinant of Hessian), γνωστή και με το ακρωνύμιο DoH. Συγκεκριμένα, η DoH αναζητά στην εικόνα περιοχές που παρουσιάζουν ισχυρές παραγώγους σε κάθετη διεύθυνση. Η μεθοδολογία στηρίζεται στον υπολογισμό του πίνακα των παραγώγων δεύτερου βαθμού της εικόνας, γνωστός ως *Εσσιανός*. Στη συνέχεια, η μεθοδολογία αναζητά σημεία (pixels) στην εικόνα όπου μεγιστοποιείται η ορίζουσα.

Η παρούσα μελέτη διερευνά την απόδοση δυο διαφορετικών μεθόδων μηχανικής όρασης και συγκεκριμένα της *circular Hough transform* (CHT) και της *determinant of Hessian* (DoH), με στόχο την αυτόματη ανίχνευση κρατήρων μετεωρητών στην επιφάνεια του πλανήτη Άρη, κάνοντας επεξεργασία σε ένα ψηφιακό μοντέλο της επιφάνειάς (ΨΜΕ)

του πλανήτη. Ειδικότερα, αυτή η εργασία περιλαμβάνει μια πιλοτική εφαρμογή της DoH στην αυτόματη ανίχνευση κρατήρων στην ειπφάνεια του Άρη. Αν και η DoH έχει εφαρμοστεί πολλάκις στο παρελθόν σε συμβατικές εικόνες (βλέπε π.χ. Grauman and Leibe, 2011), η εφαρμογή της DoH για την ανίχνευση μετεωρητικών κρατήρων σε ψηφιακό μοντέλου εδάφους υλοποιείται για πώτη φορά στα χρονικά σε αυτή την εργασία, χρησιμοποιώντας ένα αρειανό ΨΜΕ αποκτηθέν κατά τη διαστημική αποστολή Mars Global Surveyor. Συν τοις άλλοις, η απόδοση της DoH συγκρίνεται ως προς εκείνη της CHT για τα συγκεκριμένα δεδομένα.

Οι δυο τεχνικές δοκιμάστηκαν πάνω σε ένα ψηφιακό μοντέλο εδάφους του Άρη που προσφέρεται από το "Πρόγραμμα Αστρογεωλογίας" της Γεωλογικής Υπηρεσίας των Η.Π.Α. (http://astrogeology.usgs.gov/). Αυτό το ΨΜΕ έχει υποστεί κατάλληλη επεξεργασία, ώστε να είναι άμεσα για χρήση σε κοινά συστήματα γεωγραφικών πληροφοριών και έχει κατασκευαστεί από δεδομένα που συλλέχθησαν κατά τη διάρκεια του διαστημικού προγράμματος Mars Global Surveyor (MGS). Η ευρύτερη περιοχή μελέτης βρίσκεται μεταξύ του γεωγραφικού πλάτους 0º και -30º και του γεωγραφικού μήκους 30ºΕ και 60ºΕ που περιέχονται στην περιοχή *Terra Sabaea* του Άρη.

Ωστόσο, μια προσεκτική μελέτη του αρειανού ΨΜΕ αποδεικνύει πως οι κρατήρες δεν έχουν παραμείνει άθικτοι από την εποχή δημιουργίας τους. Η αρειανή ατμοσφαιρική κυκλοφορία, η πάλαι ποτέ επιφανειακή απορροή και ο συνεχής βομβαρδισμός της επιφάνειας του πλανήτη (Barlow, 2016) έχουν επιφέρει αλλοίωση, σε κάποιο βαθμό, των γεωμετρικών χαρακτηριστικών των κρατήρων. Αυτό έχει ως αποτέλεσμα την "εισαγωγή

θορύβου" κατά τη διαδικασία της αναγνώρισης. Συνεπώς, μια μέθοδος τεχνητής όρασης θα πρέπει να είναι ικανή να αναγνωρίσει μια οντότητα ακόμα και μέσα από την ατελή της παρουσία εξαιτίας του θορύβου.

Η ανίχνευση με τη χρήση της μεθοδολογίας CHT βασίζεται στον εντοπισμό ακμών κυκλικών οντοτήτων, όπως οι κρατήρες, αφού προηγηθούν πολλαπλά στάδια επεξεργασίας εικόνας, ώστε οι οντότητες που αναγνωρίζονται από το ανθρώπινο μάτι να εκπέσουν σε γραμμικές. Αυτό επιτυγχάνεται με τον υπολογισμό παράγωγης εικόνας από το αρχικό ΨΜΕ και συγκεκριμένα της καμπυλότητας του αναγλύφου, αφού έχει προηγηθεί συνέλιξη με γκαουσιανό φίλτρο για εξομάλυνση του αναγλύφου. Ακολουθεί κατωφλίωση, μορφολογικό κλείσιμο και λέπτυνση της εικόνας πριν γίνει έτοιμη για ανάλυση με την CHT.

Αν είναι γνωστό εκ των προτέρων πως οι κύκλοι της εικόνας έχουν σταθερή διάμετρο, η CHT προβάλει τα σημεία της δισδιάστατης εικόνας ως κύκλους σε έναν δισδιάστατο παραμετρικό χώρο. Αν, απ'την άλλη, οι κύκλοι έχουν μεταβλητή διάμετρο στην εικόνα, τότε η CHT θα προβάλει τα σημεία της εικόνας ως κώνους σε έναν παραμετρικό χώρο. Όσο συχνότερα τέμνονται οι κύκλοι (ή οι κώνοι αντίστοιχα) σε ένα σημείο στον παραμετρικό χώρο, τόσο πιθανότερο οι συντεταγμένες αυτού του σημείο να παραπέμουν σε κέντρο πραγματικού κύκλου στην εικόνα. Αυτή διαδικασία καλείται *ψηφοφορία* (voting). Όσο εντονότερη είναι όμως η παρουσία ανεπιθύμητων αντικειμένων στην εικόνα (θόρυβος), τόσο μεγαλύτερη είναι η συμμετοχή τους στην *ψηφοφορία*,

εκλέγοντας-παραπλανητικά- σημεία που δεν αντιστοιχούν σε πραγματικά κέντρα κύκλων στην εικόνα.

Πριν την εφαρμογή της CHT η εικόνα υπέστη κάποια επεξεργασία, ώστε όλα τα αντικείμενα της εικόνας να εκπέσουν σε γραμμές πάχους ενός φατνίου (Kim et al., 2005; Stepinski et al., 2006; Bue and Stepinski, 2007). Συγκεκριμένα, έγινε συνέλιξη με γκαουσιανό φίλτρο, ώστε να περιοριστεί σε κάποιο βαθμό ο θόρυβος. Στην συνέχεια, υπολογίστηκε η καμπυλότητα του ΨΜΕ ως η δεύτερη παράγωγος του ΨΜΕ, καθώς έτσι αναδεικνύονται καλύτερα οι ακμές των κρατήρων. Στη συνέχεια, ακολούθησαν τα εξής στάδια, όπως έχουν προταθεί από τους Bue and Stepinsky (2007): 1) κατωφλίωση με στόχο να προκύψει μια δυαδική εικόνα, 2) μορφολογικό κλείσιμο (διαστολή και διάβρωση) χρησιμοποιώντας δομικά στοιχεία διαστάσεων 3×3, και τέλος 3) λέπτυνση χρησιμοποιώντας δομικό στοιχείο 3×3.

Η κατωφλίωση της εικόνας χρησιμοποιείται ως μια προκαταρκτική διαδικασία κατάτμησης της εικόνας. Στην απλούστερη εκδοχή της, η κατωφλίωση αντικαθιστά κάθε φατνίο της εικόνας με ένα άσπρο φατνίο, εάν η ένταση του φατνίου είναι πάνω από την τιμή κατωφλίωσης και με μαύρο φατνίο αν η τιμή της έντασης που αντιστοιχεί σε εκείνο το φατνίο είναι κάτω από την τιμή κατωφλίωσης.

Το μορφολογικό κλείσιμο περιλαμβάνει διαστολή της εικόνας χρησιμοποιώντας δομικό στοιχείο και στη συνέχεια διάβρωση της εικόνας με το ίδιο στοιχείο. Η διαστολή αποσκοπεί στη διόγκωση των αντικειμένων της εικόνας (άσπρα φατνία) πληρώνοντας

μικρά κενά που εμφανίζονται ανάμεσα στα αντικείμενα. Στη συνέχεια, η διάβρωση αποτελεί τη μαθηματικώς αντίστροφη διαδικασία, κατά την οποία ένα δομικό στοιχείο συνελίσσεται με τη δυαδική εικόνα προκαλώντας την συστολή του πάχους των αντικειμένων. Συνεπώς, η διαδικασία του μορφολογικού κλεισίματος επιτυγχάνει την αναπλήρωση των ατελειών των ατελών αντικειμένων, διατηρώντας το πάχος τους μικρό. Στη συνέχεια, ακολούθησε η ανάδειξη των ακμών με λέπτυνση, κατά την οποία όλα τα γραμμικά αντικείμενα της εικόνας εκπίπτουν σε γραμμές πάχους ενός φατνίου.

Ακολούθησε εφαρμογή της CHT σε περιβάλλον Matlab χρησιμοποιώντας τον αλγόριθμο *CircularHough_Grd*, σχεδιασμένο για Matlab. Ωστόσο, ο αλγόριθμος *CircularHough_Grd* προσδιόρισε κέντρα κύκλων σε θέσεις που σπάνια αντιστοιχούσαν σε κέντρα κρατήρων. Αυτό το αποτέλεσμα αποδίδεται στο θορυβώδη χαρακτήρα της επεξεργασμένης εικόνας. Η εφαρμογή της τυπικής εκδοχής της CHT στο αρειανό ΨΜΕ δεν είχε επιτυχία, καθώς η παρεμβολή άσχετων γειτονικών οντοτήτων, τα οποία εξακολούθησαν να υπάρχουν στην εικόνα και μετά την επεξεργασία, εισήγαγε επιπλέον θόρυβο και οδήγησε στην εμφάνιση ψευδών σημάτων (οντοτήτων). Τουναντίον, δημοσιευμένες παραλλαγές της μεθοδολογίας CHT περιλαμβάνουν εξουθενωτικές διαδικασίες επεξεργασίας εικόνας για να περιορίσουν την επίδραση του θορύβου, και για τον λόγο αυτό, αυτές θεωρήθηκαν ως μή-πρακτικές για εφαρμογές ρουτίνας.

Εναλλακτικά, ο εντοπισμός κρατήρων διεξήχθει μέσα από την προσέγγιση των blobs, χρησιμοποιώντας τον αλγόριθμο *blob_doh* που είναι σχεδιασμένος για την γλώσσα προγραμματισμού Python. Πριν την εφαρμογή του αλγορίθμου *blob_doh* η εικόνα

υπέστη ελάττωση θορύβου, συνελίσσοντας γκαουσιανό φίλτρο. Όταν η *blob_doh* εφαρμόστηκε σε τμήματα του ΨΜΕ που ήταν σχετικά επίπεδα (όπως αποκάλυψαν οι αντίστοιχες τοπογραφικές τομές) τα ποσοστά επιτυχίας της ανίχνευσης κρατήρων ήταν αξιόλογα, της τάξης του 88%.

Ωστόσο, όταν η *blob_doh* εφαρμόστηκε σε πιο περίπλοκες τοπογραφίες, χαρακτηριζόμενες από ημιτονοειδή διακύμανση και κλίση, τα αποτελέσματα ήταν λιγότερο ικανοποητικά. Αν και η *blob_doh* κυκλώνει σχεδόν όλες τις «αρνητικές» τοπογραφικές ανωμαλίες (πραγματικοί κρατήρες) σε αντίθεση με την περίπτωση του σχετικά επίπεδου ΨΜΕ όπου απαντούν μόνο «αρνητικές» τοπογραφικές ανωμαλίες (κρατήρες), στο ημιτονοειδές και κεκλιμένο ΨΜΕ ο αλγόριθμος κυκλώνει (εξ'ορισμού) και τις «αρνητικές» και τις «θετικές» τοπογραφικές ανωμαλίες (ψευδείς κρατήρες-εξάρσεις). Οι ψευδείς κρατήρες είναι ανεπιθύμητοι.

Ένας τρόπος για να παρακαμφθεί η παρεμβολή των «ψευδών κρατήρων», ήταν να αποκοπούν οι πολύ υψηλές τιμές έντασης από την εικόνα, ώστε να εμποδισθεί η *blob_doh* από το να κυκλώσει «φωτεινά» blobs. Με αυτόν τον τρόπο, ναι μεν επιτεύχθησαν να απομονωθούν οι ψευδείς κρατήρες, αλλά από την άλλη ή απόρριψη των υψηλών τιμών της εικόνας, είχε ως αποτέλεσμα να απορριφθεί το 50% περίπου της επιφάνειας της εικόνας, χάνοντας όσους κρατήρες κείτονταν σε τοπογραφικά υψηλές περιοχές. Παρόλα αυτά, το ποσοστό επιτυχίας της DoH παρέμεινε υψηλότερο από εκείνο της CHT, ακόμα και στην περίπτωση του περίπλοκου αναγλύφου.

Συνολικά, ως υποκατάστατο της CHT, η μεθοδολογία DoH φάνηκε να έχει καλύτερα αποτελέσματα, ανιχνεύοντας τη μεγάλη πλειοψηφία κρατήρων που απαντούν σε σχετικά επίπεδες περιοχές του αρειανού φλοιού, με το ποσοστό επιτυχίας να αγγίζει το 88%. Ωστόσο, το ποσοστό επιτυχίας της τεχνικής επιδεινώθηκε όταν η DoH εφαρμόστηκε σε πιο περίπλοκες τοπογραφίες της επιφάνειας του πλανήτη. Μολατάυτα, συνολικά η DoH είχε καλύτερα αποτελέσματα από την CHT παρά την πολυπλοκότητα του αναγλύφου, γιατί η DoH αποδείχθηκε λιγότερο ευαίσθητη στο θόρυβο απ'οτι η CHT. Τα παρόντα αποτελέσματα, αν και όχι βέλτιστα, ενθαρρύνουν μελλοντική έρευνα για τη βελτίωση των επιδόσεων της DoH σε εφαρμογές ρουτίνας που απαιτούν ανίχνευση κρατήρων σε πλανήτες του ηλιακού συστήματος.

**Λέξεις κλειδιά:** μετεωρητικοί κρατήρες, ανίχνευση ακμών, ανίχνευση περιοχών, ορίζουσα του Εσσιανού πίνακα

**List of Contents** **page**

**List of Figures** **page**

## 1. Introduction

Frequency counting of impact craters on terrestrial planets and moons of the Solar System is an essential means of relative geochronology of the upper planetary crust (Hartman et al., 2001; Carr et al., 2010), as well as probing into paroxysmal phases of meteor showers in the early Solar System (Gomes et al., 2005).

Numerous spaceborne surveying and remote sensing missions to Mars (Pyle, 2012) over the last decades have acquired digital elevation data for the entire planet at usable resolutions, enabling planetary geologists to carry out morphometric analysis of the Martian meteor craters (Brunetti et al., 2014). However, counting of myriads of impact craters manually is a tedious and time-consuming task.

Subjects of research in geology, and consequently in astrogeology, involving the reconstruction of original landforms from their current remnants, can be dealt with if they are reduced to morphological, and eventually geometrical, problems (Bayer, 1985). Such problems can be dealt with by computer algorithms operating on digital terrain models (DTM). Hence, impact crater detection through computer vision methods may be extremely practical in astrogeology as it can automate, and thus expedite, the crater-counting procedure. Computer vision (also known as image understanding) is a branch of computer science aiming at replicating biological (human) vision through appropriate algorithms at different levels so that certain image components (objects) can be detected/recognized by computers.

Nevertheless, planet surface processes (Berman et al., 2009) may induce random and persistent disturbance (noise) to the original structure (signal) over the course of time, resulting in the gradual deformation of the original landform. This is particularly the case of the Martian impact craters whose edges have experienced some degree of erosion by the former Martian hydrological cycle (Andrews-Hanna et al., 2007).

Circular Hough transform (CHT) has been promoted as a method for the detection of impact craters (Kim et al. 2005; Stepinski et al., 2006; Bue and Stepinski, 2007). CHT (Illingworth and Kittler, 1987) is an adaptation of Hough transform (e.g. Xiao and Weij, 2006; Mingzhu and Huanrong, 2008). It is a feature detection method that exploits the edges of circular objects in an image to reconstruct their perimeter out of their imperfect instances. This is achieved through a voting procedure from the 2D space of the imagery to a 2D or 3D parametric space.

Nevertheless, the present state of impact craters on mars can be very noisy as degradation may have deformed their edges during the geological time. Therefore the actual edge of a heavily eroded crater will be expected within a specific probability within a given area around its center. Recognition may become even more problematic when neighborhoods of different edges start to intersect. In these cases intersecting edges cannot be reconstructed accurately (Bayer, 1985).

Another way to go around the problem of imperfect crater instances (which may render edge-detection methods ineffective) is region-based detection. *Blob* detection (Kaspers,

2011) utilizes operators capable of delineating regions that exhibit uniform properties. Therefore blob detection is not affected by imperfections of linear components such as the eroded crater edges. Among various blob detection methods (Kaspers, 2011), the *determinant of Hessian* (Lindeberg, 1993, 1998) is well-known. Specifically, the determinant of Hessian (*DoH*) looks for locations on the image that demonstrate strong derivatives in perpendicular directions. The technique takes advantage of the matrix of the second-order derivatives of the image, known as the *Hessian*.

This work is a pilot application of DoH for impact crater detection on Mars. Although blob detection has been applied to numerous cases involving conventional images (e.g. Grauman and Leibe, 2011) and satellite imagery (Karantzalos and Argialas, 2004) this is, to our knowledge, the first application of DoH for impact crater detection on a digital terrain model. This work undertakes to test DoH on a Martian DTM acquired during the Mars Global Surveyor mission. The performance of DoH is also compared to that of CHT.

## 2. Background

### *2.1. Impact craters of Mars*

Impact cratering on rocky planets and moons dates back to the dawn the Solar System, over 4 billion years (gigayears, Ga) ago (Claeys and Morbidelli, 2011). Meteor craters are created by collision of interplanetary debris (meteorites, asteroids or comets) with the planetary crust. Although resurfacing processes on the Earth (e.g. plate tectonics, erosion and sedimentation) have erased much of the primordial impact record, on planets such as Mercury, Mars and the Moon, where intense geological activity ceased earlier, the scars of ancient meteorite bombardment have been preserved for longer time-scales.


*Fig. 2.1. Impact craters on Mars overlapping with relict drainage network*

A major proportion of cratering on Mars is associated with the *Heavy Late Bombardment* (LHB) in the early Solar System (Claeys and Morbidelli, 2011), which is an astronomical

event of cataclysmic dimensions that occurred 4.1-3.6 Ga ago. During this event a massive amount of meteorites collided with the Earth-like planets of the inner Solar System (i.e. Mercury, Venus, Mars) and the Moon (Claeys and Morbidelli, 2011) leading to the well-known mottled appearance of their crust surface.

Martian impact craters exhibit a broad diversity of types. The weathering influence of the Martian atmosphere, and the former hydrological cycle (Fig. 2.1), have acted as substantial moderators of the crater morphology. Martian craters crop up in a broad range of sizes. Documented craters with diameters exceeding 5 km are estimated to be substantially more than 42,000 (Barlow, 1988). These numbers grow geometrically for smaller craters. There is a striking difference in crater density between the planet's latitudinal hemispheres, with the southern hemisphere exhibiting a substantially greater number of craters than the northern hemisphere.

*2.2. The recognition problem*

Computer vision tasks employ algorithms to recognize 3D objects in 2D images whose properties are known *a priori*. Several methodologies for object detection have been developed, depending on the nature of the features to be detected. These can be grouped in two major categories, namely the *edge-based* methods and the *region-based* methods, depending on whether the algorithms deal with linear or areal properties.

Both approaches require that a mathematical model of the features concerned be conceived on the basis of the feature geometry and spatial properties. Then, the

methodology should present a stepped procedure (algorithm) capable of reconstructing, within a degree of tolerance, the shape by taking into account the instances of the objects. Because noise may be added to the image, an effective feature detection technique should be designed in such a way that its results are not skewed by the presence of noise.

As far as the *edge-based* family of techniques are concerned, the *circular Hough transform* (e.g. Argialas and Krishnamurthy, 1992; Xiao and Weij, 2006; Mingzhu and Huanrong, 2008) and the *ellipse and line segment detector* (Pătrăucean et al., 2012), known as ELSD, are the most noteworthy examples. Particularly, Circular Hough Transform (CHT) is most celebrated in computer vision applications such as magnetic resonance imaging (e.g. Zhong et al., 2014), iris recognition (e.g. Verma et al., 2012) and biometry (e.g. Prakash and Rajesh, 2008). CHT is a variance of the Hough transform (Duda and Hart, 1972). The Hough transform facilitates the detection of primitives such as lines circles and ellipses. The philosophy behind CHT is the construction of a parameter space where the coordinates vote for the parameters being searched in the image space.

Regarding the *region-based* group of detection methods, these perceive the intensity fluctuations in the image as a succession of basins and hills and, hence, an object can be simulated by either way. A traditional means of extracting objects through the basin/hill perception is the *watershed segmentation* (Beucher and Lantuéjoul, 1979). Watershed segmentation mimics the process of rain water filling the basins while it is flowing along the hill slopes until the basins become full of water (*flooded* image). When the procedure

is completed, basin-like objects will appear as monochrome compact regions while hill-like objects will crop up as lighter-colored regions.

If *topographic* fluctuations in the image can be simulated as bell-shaped surfaces (upright or inverted) then the term *blob* may be applied. Lindeberg (1993) defines blobs as local extrema of approximately Gaussian functions. Watershed and blob detection methods have been widely applied to numerous case studies ranging from the detection of boundaries of mineral grains in geological thin sections (Barraud, 2006) to cell detection in biological tissue (Li et al., 2007).

Planetary scientists undertaking studies on extraterrestrial DTMs have made use of CHT (Bue and Stepinski, 2007) and watershed segmentation (Bue and Stepinski, 2007, Fig. 4a therein) to facilitate meteor crater detection. Nevertheless, both approaches have faced serious shortcomings. Regarding watershed segmentation, not all resulting basins will correspond to craters, but also to irrelevant depressions. In addition, in cases where craters have been exhumed in the interior of larger craters they will be masked by the "flood" and become merged with the larger crater.

So far as CHT is concerned, the noisy nature of the DTMs involved inevitably introduces votes from irrelevant objects, frequently leading to the emergence of false (*ghost* or *phantom*) craters. Only very meticulous image pre-processing, such as fragmentation of the original image into numerous smaller images (Bue and Stepiknski, 2007) may reduce the noise in the crater neighborhood. This study aims to explore the potential of the so far

untested blob detection operators for impact crater extraction and to contrast its results to those by CHT.

# 3. Methodology

## *3.1. Hough Transform*

Hough Transform involves switching back and forth from the 2D image space *(x,y)* to a multi-dimensional space (depending on the number of the curve parameters), known as the parametric space, from which object candidates are detected as local maxima of votes cast into the so-called accumulator matrix. Such a parametric space is known as the "Hough" space (Duda and Hart, 1972; Argialas and Krishnamurthy, 1992), and its dimensions are designated by the number of parameters involved (e.g. 2D for lines, 3D for circles etc). The manuscript proceeds with an introduction to the Linear Hough Transform (LHT), which provides the fundamentals to understand the higher-parameter Circular Hough Transform (CHT) methodology thereinafter.

### *3.1.1. Linear Hough Transform*

In case of a line $y = mx + c$, with $m,c$ corresponding to the slope and the offset respectively (Fig.3.1), the Hough space is two dimensional $(m,c)$ and the line $y = mx + c$ plots as a point in Hough space $(m_0,c_0)$. Conversely, a given point $(x_0,y_0)$ in the image space would correspond to a line in the Hough space (Fig.3.2). The infinite number of lines crossing that point are characterized by infinite pairs of $(m,b)$ which fulfill equation $c = y - m_0x$. The linear relationship between $c$ and $m$ means that the parameters plot as a line in the Hough space.

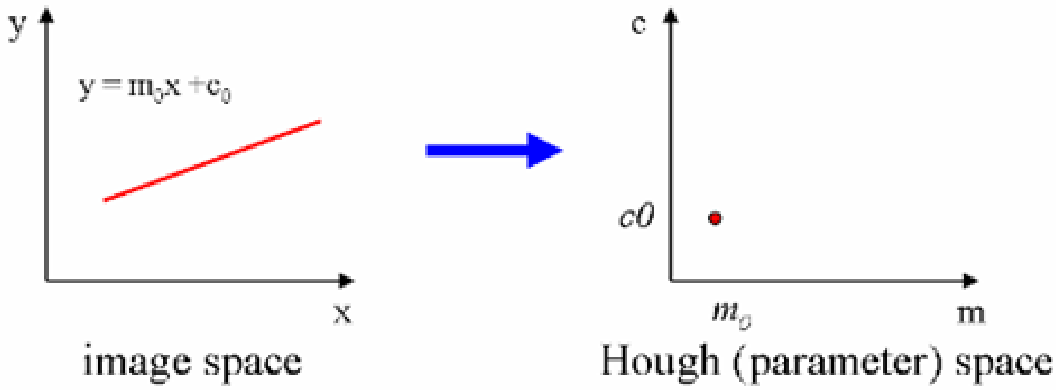


*Fig. 3.1. A line in image spece corresponds to a point in the 2D Hough parameter space (from Grauman, 2014).*

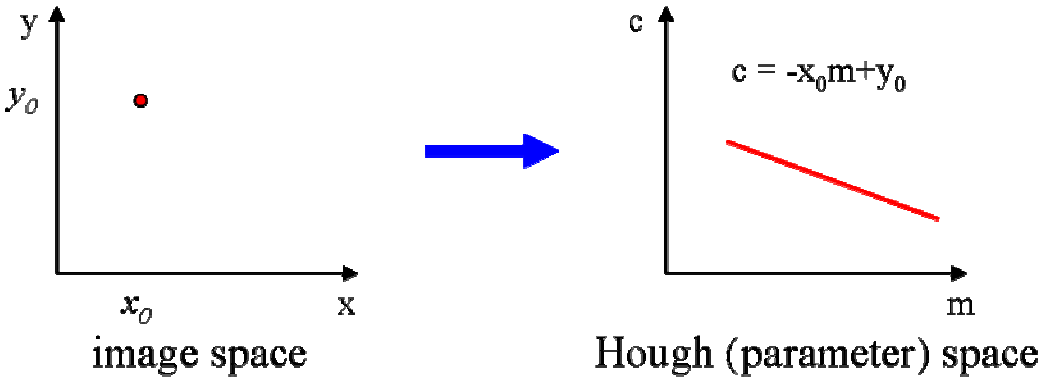


*Fig. 3.2. A point in the image space corresponds to a line in the Hough parameter space (from Grauman, 2014).*

In order to calculate the line that passes through two known points, i.e. the parameters *m* and *b* of the line being sought, the points are plotted as lines in the Hough space and their intersection coordinates reveal the parameters of the line being sought (Fig.3.3). The coordinates are calculated by solving the system of equations $c = -x_0m+y_0$ and $c=-x_1m+y_1$.

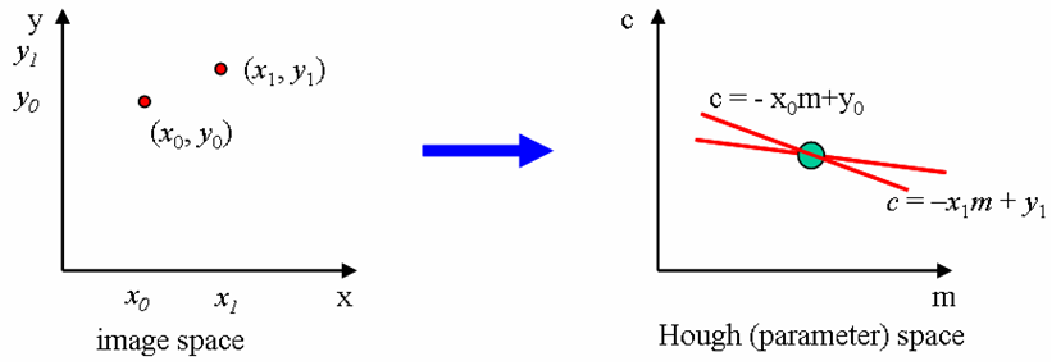


*Fig.3.3. The line passing through two points in the image space is the solution of the intersecting lines in Hough space (from Grauman, 2014).*

For a larger set of collinear points (Fig.3.4) from the image space, each pair of points is plotted as a line in the parametric space. If the parametric space is gridded, the higher the intersections strike in a bin the more likely this bin will contain the *c* and *m* parameters of the line passing through the points on the image space. This procedure is called *voting* as each intersecting line in the parametric space votes for line parameters that define a line in the image space.

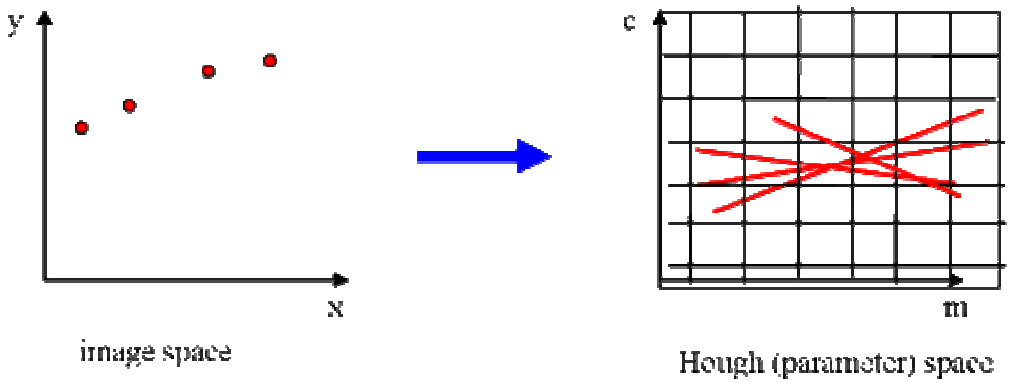


*Fig.3.4. The parameters describing a line passing through collinear points correspond to a local maximum of votes cast in the accumulator array (from Grauman, 2014).*

However, as vertical lines are associated with infinite tangents the *hessian* form for the line is preferred: $r = x\cos\theta + y\sin\theta$, where $r$ is the distance from the origin and $\theta$ the angle from the horizontal axis. In that case, the parametric space is defined by the angle and the distance from the origin ($r$, $\theta$) instead of the slope and the offset.

In this alternative form, parameters $r,\theta$ are estimated in the Hough space in a different fashion. Consider, for example, the supposedly collinear points of Fig.3.5. For a given data point a number of lines are drawn through it, each at different angle (solid lines in Fig. 3.5). Each solid line is then intersected by another vertical line (dashed lines in Fig.3.5) passing through the origin.

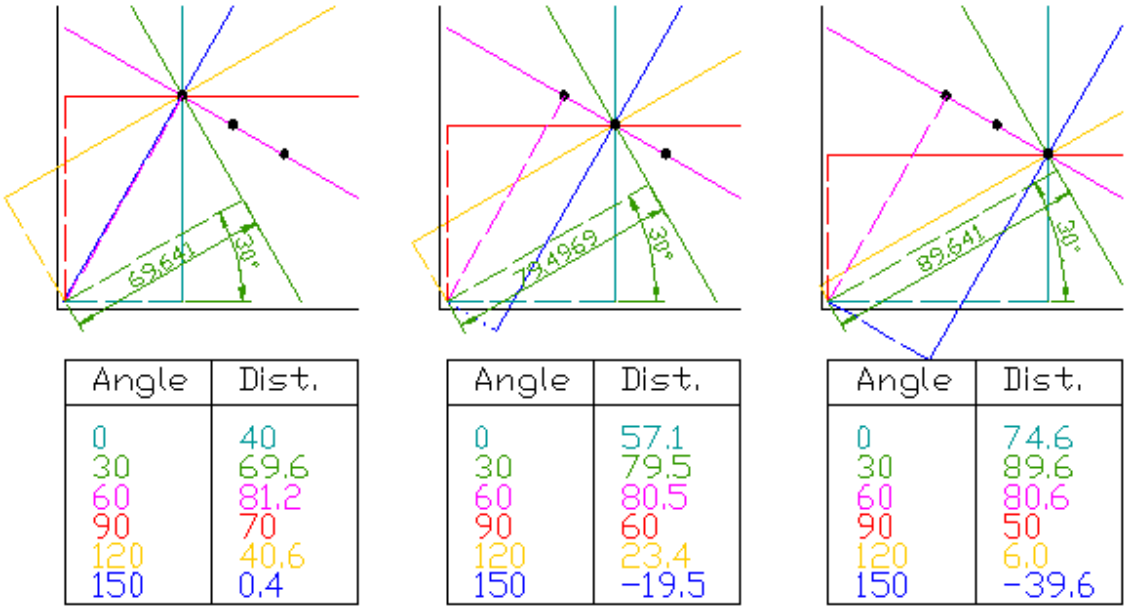


| Angle | Dist. |
|---|---|
| 0 | 40 |
| 30 | 69.6 |
| 60 | 81.2 |
| 90 | 70 |
| 120 | 40.6 |
| 150 | 0.4 |

| Angle | Dist. |
|---|---|
| 0 | 57.1 |
| 30 | 79.5 |
| 60 | 80.5 |
| 90 | 60 |
| 120 | 23.4 |
| 150 | −19.5 |

| Angle | Dist. |
|---|---|
| 0 | 74.6 |
| 30 | 89.6 |
| 60 | 80.6 |
| 90 | 50 |
| 120 | 6.0 |
| 150 | −39.6 |

*Figure 3.5. Alternative voting procedure for line detection exploiting the hessian form of the line. Parameters are angle of intersection and distance from the origin (source: Wikipedia).*

The length (i.e. the perpendicular distance to the origin) and the angle of each dashed line are then measured. The procedure is repeated for each datapoint, and the pairs of the results are shown in the accompanying tables. Therefore, the parametric space is now defined by distances and angles.

Each point from the image space now plots as a curved line defined by the angle/distance pairs (Fig.3.6a). Each line corresponds to a vote. The intersection of the curves defines the wanted $r,\theta$ parameters. If the graph shown in Fig.3.6a. is gridded then it can be illustrated in the form of a raster graph, known as the *accumulation matrix* (Fig.3.6b).

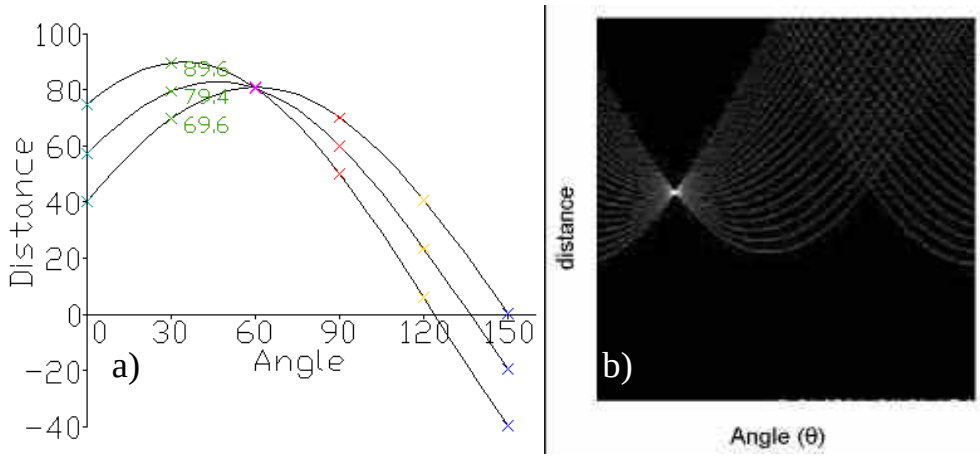


*Fig. 3.6. a) Parametric representation of points as curves in the 2D Hough space. b) accumulation matrix illustrating the higher incidence of curve intersection (source Wikipedia).*

### *3.1.2. Circular Hough Transform*

The Hough transform can be used to determine the parameters of a circle when a number of points of its perimeter are known. Circular Hough Transform (CHT) exploits the circle formula (Eq.1) to calculate triplets of parameters ($a,b,r$) which satisfy Eq.1 when they are

combined with the coordinates (*x,y*) of at least three points in the image-the necessary and sufficient condition for drawing a circle.

$$(x_i - a)^2 + (y_i - b)^2 = r^2 \qquad \text{Eq.1}$$

Parameters *a,b* can be expressed as a function of the coordinates of a (*x,y*) point on the perimeter of the circle (Fig. 3.7) and its diameter *r* as: $x = a + R\cos(\theta)$ and $y = b + R\sin(\theta)$. Estimation of triplets of parameters is achieved through the transformation of points from the biaxial image space into geometric elements in a triaxial (*a,b,r*) parametric space (Fig.3.8).

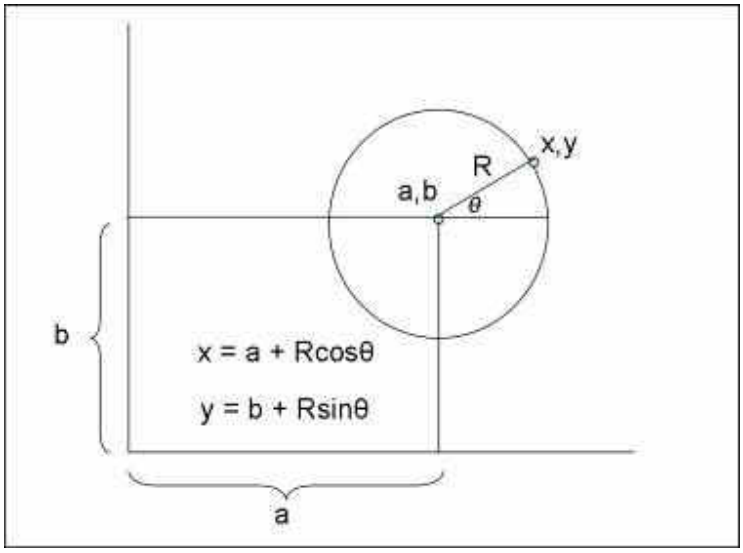


*Fig. 3.7. The circle formula expressed as a function of the center (a,b) coordinates, the radius (R) and the angle of the radius (θ).*

For a given *r*, points from the image space can be transformed through the circle formula into circles in the 3D Hough space. When the radius moves along the *r* axis then a point from the image space will plot as a cone in the parametric (Hough) space.

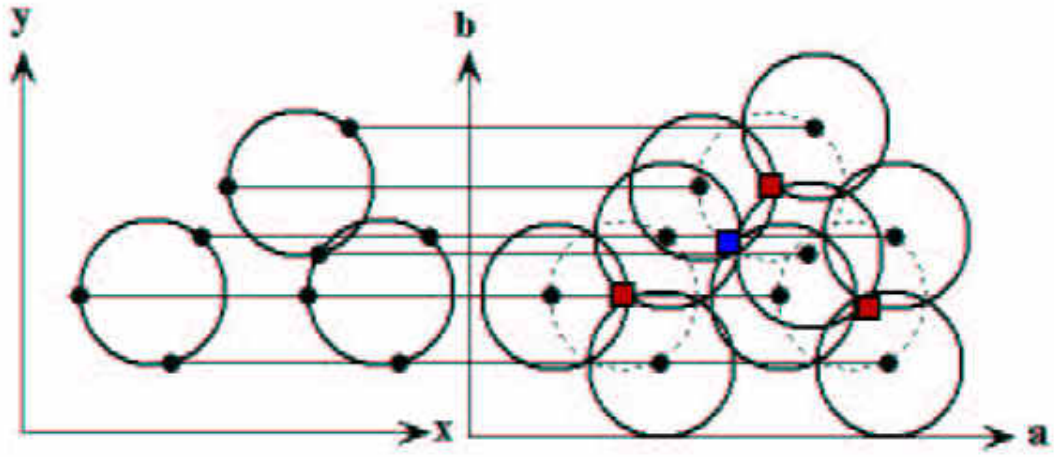


*Fig. 3.8. Transformation of circles from the image space (left) to the Hough space for a given radius.*

Circle candidates in the image space are obtained as local maxima (candidate circle centers) of cone intersection counts in the accumulator matrix, resulting from the voting procedure carried out in a parameter space.

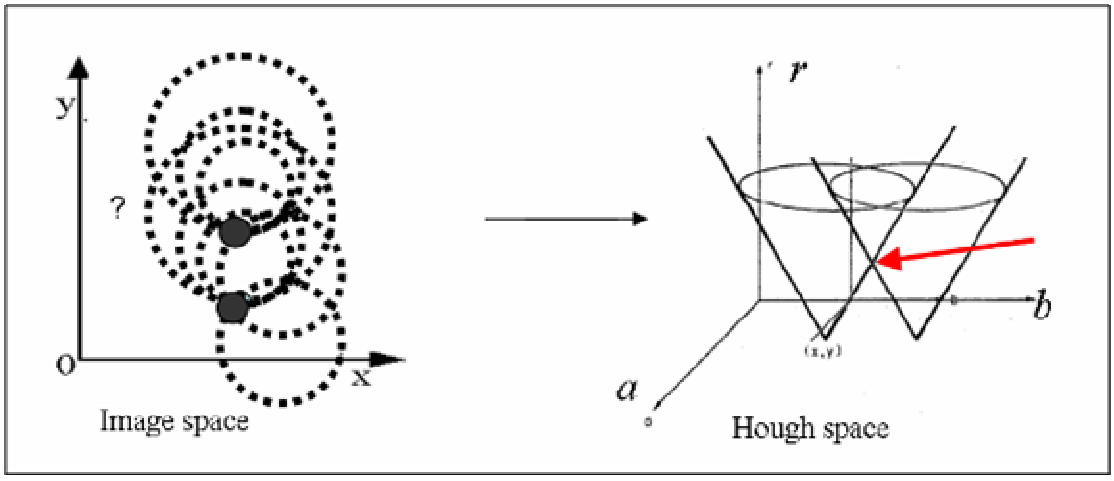


*Fig. 3.9. Transformation of circles from the image space (left) to the 3D Hough space (right) for variable radiuses.*

In principle, the voting procedure involves counting the votes within a range of radiuses (several horizontal plains in 3D Hough space) and the higher the cone intersections strike

in a bin of the *a*×*b* matrix the more likely the cell's a,*b* coordinates map out the center of an actual circle in the image (Fig.3.9).

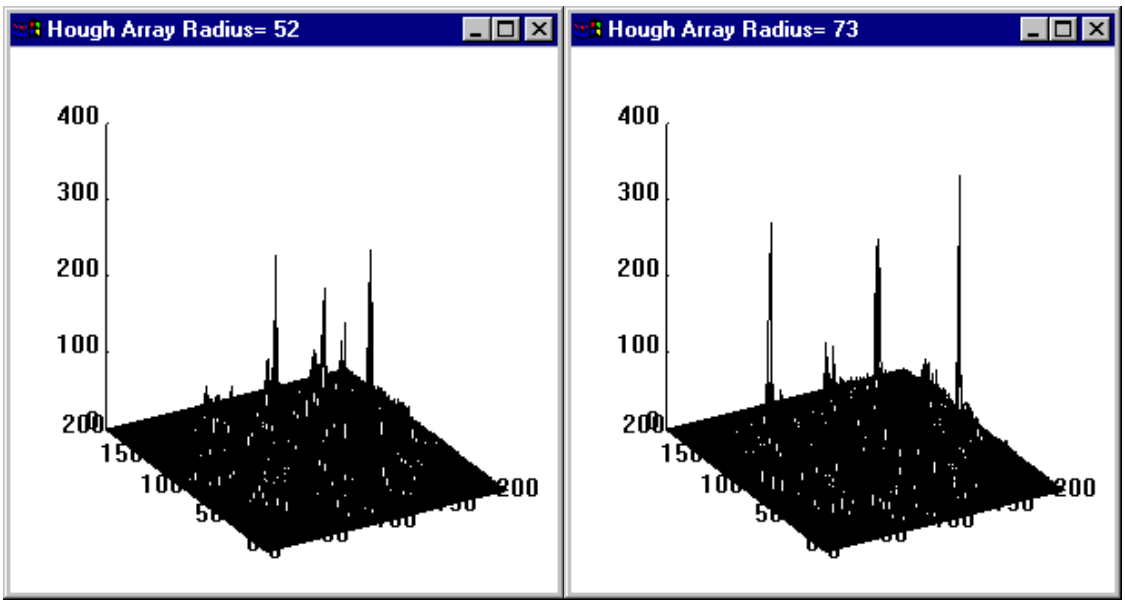


*Fig. 3.10. Accumulator array for two different radiuses (from Rhody, 2005).*

Prominent peaks correspond to circle centers (Fig.3.10). It is understood that if the search radius changes the distribution of peaks will vary also. It is possible that spurious centers appear, resulting in phantom instances-they can be removed by matching to actual image. Hough become evident.

Hough circle transform requires some amount of image pre-processing so that the circle edges mark out. The profile curvature is typically calculated to reveal the edges. Then a threshold is set to the gradient magnitude so as to convert the grey-scale image into black and white (binary image). A step including morphological opening and skeletonization of the image is usually interposed. In that way only foreground pixels with high gradient are

designated for casting votes. Basic steps of the CHT algorithm are illustrated in the following flow chart (Fig.3.11).

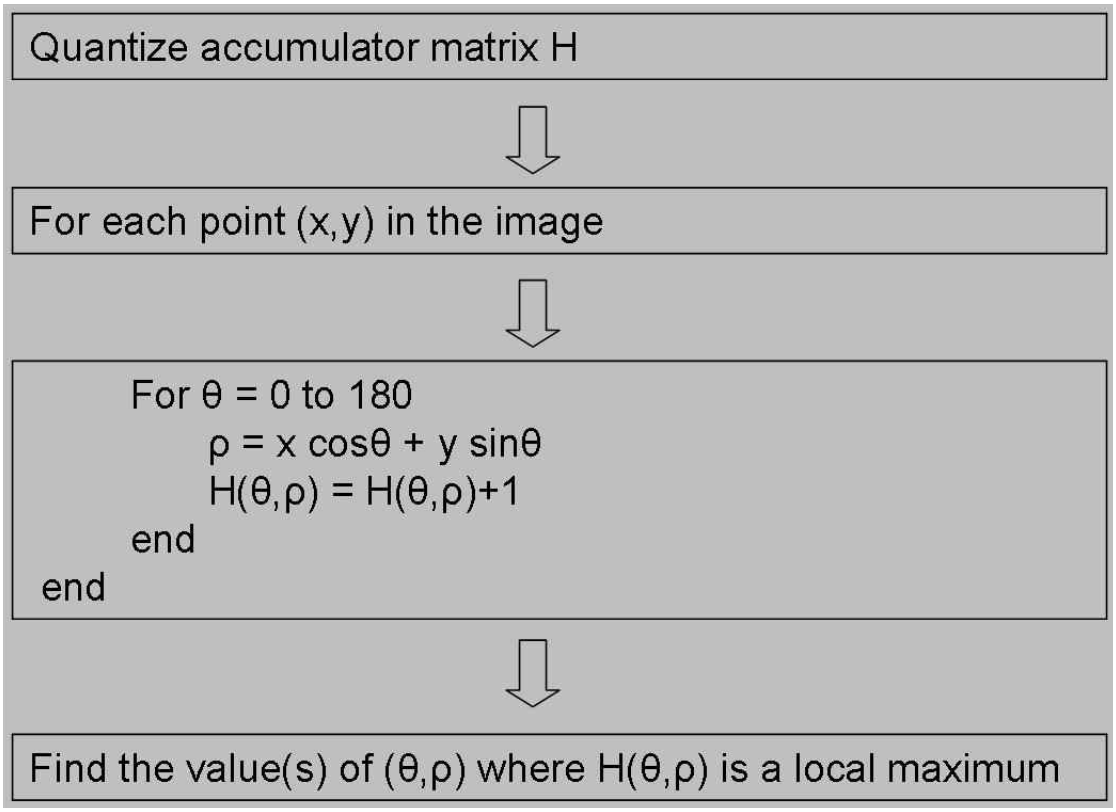


*Fig.3.11. Flow chart of the CHT algorithm in simple form*

*3.2. Blob detection through the scale-space theory perspective*

In computer vision research, blobs refer to regions in an image whose brightness differ from their surroundings (Lindegerg, 1993, 1998; Mikolajczyk and Schmid, 2004). Contrary to the edge detection methods, blob detection extracts information from regions in an image that cannot be obtained from edge detectors (*cf.* CHT). There are several definitions of blob (Kaspers, 2011). In the case of DTM-processing a blob may be described by the definition of Lindeberg (1993, 1998) according to which a blob corresponds to a region associated with a local extremum, either a maximum or a minimum (e.g. a bright blob on a darker surrounding or a dark blob on a brighter surrounding).

Blobs are detected by employing operators that detect the gradient fluctuations on an image. If the image is viewed as a function defined by three variables *f(x,y,z)* where *x,y* the coordinates and *z* the image intensity, then the gradient is a vector defined by the partial derivatives of *f*:

$$\vec{\nabla} f(x,y,z) = \langle \frac{\partial f}{\partial x}(x,y,z), \frac{\partial f}{\partial y}(x,y,z), \frac{\partial f}{\partial z}(x,y,z) \rangle \qquad \text{Eq. 2.}$$

Recognition of geological patterns often involves a broad spectrum of instabilities and deformations under variable scales of observation. Structural stability is essential for perceiving and classifying objects (Bayer, 1985). In contrast to the mathematical perception where lines and points remain stable at all scales of observation, in natural

world, objects manifest themselves in different ways which depend on the observation scale, a fact with significant consequences to image and signal processing with automatic techniques.

Blob detection procedures are amenable to the so-called *scale-space theory* (Witkin, 1983; Koenderink, 1984; Lindeberg, 1993, 1998), which constitutes a set of axioms for the representation of signals and images at multiple scales in a manner that would allow to comprehend the structure of the image (or the signal) "*at all levels of resolution and link images at successive scales. The scale at which a maximum over scales is attained will be assumed to give information about how large a blob is*" (Kaspers, 2011). In scale-space theory (SST) the representation of an image $f(x,y)$ corresponds to a one-parameter family of derived (smoothed) images $L(x,y,t)$, defined by the convolution of $f(x,y)$ by the Gaussian filter:

$$g(x, y; t) = \frac{1}{2\pi t} e^{-(x^2+y^2)/2t} \qquad \text{Eq.3.}$$

where the parameter $t \geq 0$ corresponds to the scale parameter, i.e. the successive levels of scaling, and is equal to the standard deviation of the Gaussian kernel ($\sigma^2$). For $t = 0$, $L(x,y,t) = f(x,y)$ and as $t$ increases $L$ corresponds to a progressively smoothed version of $f$. Overall, this method aims at suppressing finer texture and it is supposed that structures of width $\leq \sqrt{t}$ have been smoothed out at scale $t$.

Smoothing should be carried out in such a way that convolution does not induce spurious structures as the scale coarsens. SST claims that the Gaussian kernel is the approved

means of producing a linear scale-space. SST postulates the *topological stability* of the objects, also known as *structural stability* (Bayer, 1985), meaning that the pattern should remain practically unchanged under disturbances that may be induced by varying scales of observation (Lindeberg, 1993, 1998). SST is concerned with constraining the range of scales at which objects appear structurally stable before further processing. This qualitative information is obtained through a type of representation known as *scale-space primal sketch* (Lindeberg, 1993, 1998).

In the absence of any prior knowledge of the objects, SST advances that image processing will deliver significant structures if executed in a bottom-up fashion so that image structures can be detected in a reproducible way, from low-level analysis to abstraction, irrespective of transformations that may occur such as rotation, deformation and scaling (Grauman and Leibe, 2011). Therefore, at fine scales only tiny blobs or blob-like noise will be detected. Successive coarsening of the scale through pixel merging achieved by convolutions with the Gaussian kernel will progressively suppresses the subtle structures leading to the detection of meaningful objects, as local extrema, that emerge as simplifications of the original objects (Lindeberg, 1993, 1998; Kaspers, 2011).

There are two common approaches to blob detection, the *Laplacian of Gaussian* (Mikolajczyk and Schmid, 2001) and the *Determinant of Hessian* (Lindeberg, 1998) operator. Both aim at detecting either convex or concave structures in an image. Because of the apparent resemblance between the graphical representation of the Determinant of Hessian (*DoH*) and the crater geometry (impact craters resemble 3D, inverted Gaussian-

like depressions) it is the *DoH* operator that is here tested on the DTM from the Mars Global Surveyor.

The Determinant of Hessian searches the image for locations that display intense derivatives in orthogonal directions (Grauman and Leibe, 2011). The detector calculates the second-order derivatives of the scalar-valued "function" of the image at a pixel X = (*x*,*y*) and at scale $\sigma$ which can be represented by the commonly-named *Hessian* matrix (Eq.4),

$$H(X,\sigma) = \begin{bmatrix} L_{xx}(X,\sigma) & L_{y\chi}(X,\sigma) \\ L_{xy}(X,\sigma) & L_{yy}(X,\sigma) \end{bmatrix} \qquad \text{Eq.4}$$

where $L_{xx}$ (X, $\sigma$) is the convolution of the Gaussian second order derivative $\frac{\partial^2 f}{\partial x^2} * g(\sigma)$ and so forth. Then the method searches for pixels where the determinant of *H* (Eq.5), simply known as the *Hessian*, is maximized (Grauman and Leibe, 2011; Bay et al., 2008):

$$\det(H) = L_{xx}L_{yy} - L_{xy}^2 \qquad \text{Eq.5}$$

Fig.3.12. presents a simplified version of a blob detection algorithm according to Ming and Ma (2007).

```
Input: F(x,y),q0, σ0, s {F(x,y) is the image, q0 is threshold of roundness}
Output: R {R is the set of detected blobs}
  1. Initialize setting, a blob set R = NULL
  2. Extract blob points
  3. Compute automatic scales, get the result of detected blobs: set B
  4. Compute ζ(B)
  5. For all b ∈ B do
          if q > q0 and C(b) = ζ(B) then
          b is an interesting blob, append b to R
          end if
          Return R
     end for
```

*Fig.3.12. Simplified algorithm for blob detection. For a detailed explanation of the parameters see Ming and Ma (2007).*

## 4. Source data and photointepretation

If seen from south to north, the generalized terrain map of Mars demonstrates an abrupt decrease in the frequency and the size of the impact craters in flat areas (*planitia*) around the North Pole (Fig.4.1). Relatively smooth areas also occur in the western extremes of the western hemisphere for geological reasons that lie beyond the scopes of this study.

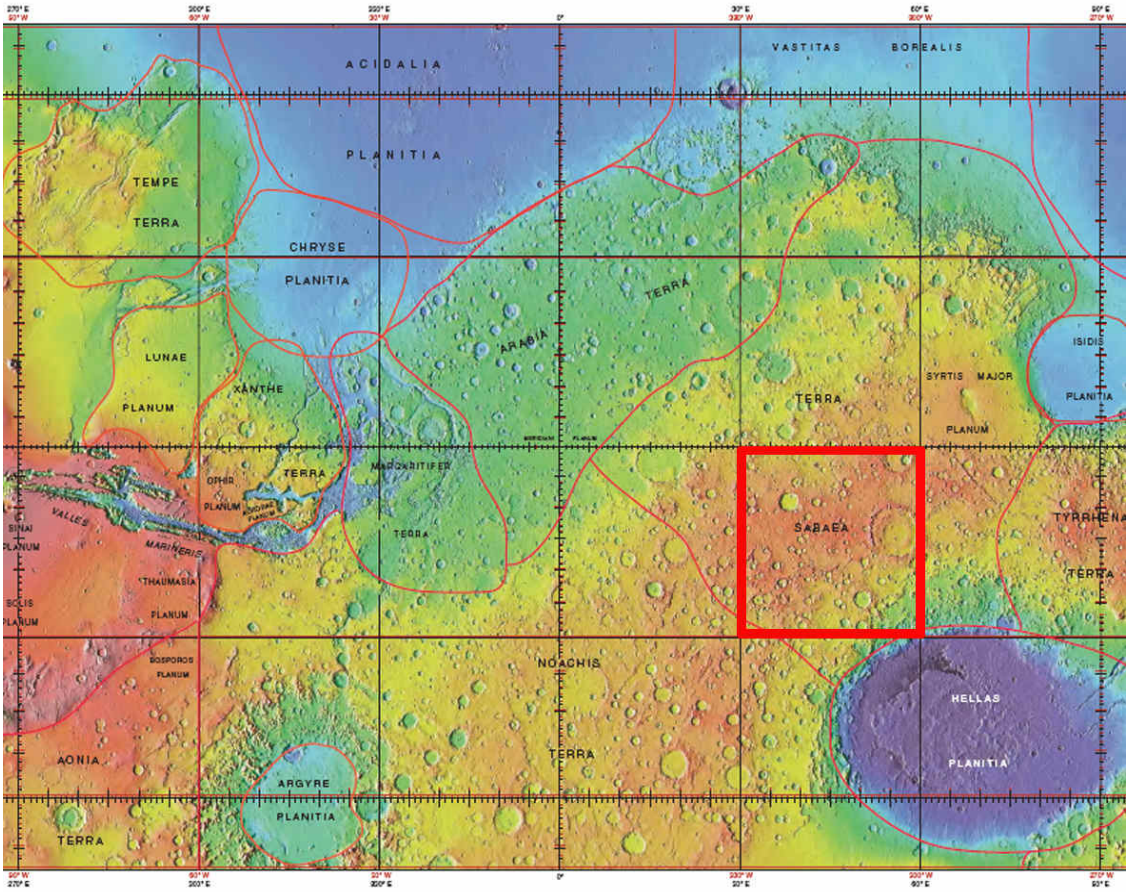


*Fig.4.1. Excerpt from the MOLA terrain map of Mars centered on the equator and the prime meridian. Red rectangular marks out the study area. (a NASA image modified by Jim Secosky http://planetarynames.wr.usgs.gov/images/mola_regional_boundaries.pdf).*

For this reason, the selection of the study window in the crater-perforated region of Mars was more or less arbitrary, and is shown in Fig.4.2. The study area captures a segment of

the equatorial area of Mars bound between latitudes: 0º and -30º and longitudes 30º and 60º. According to the USGS Astrogeology Research Program (http://astrogeology.usgs.gov/) this window mainly captures the northern parts of the *Sinus Sabaeus* quadrangle (Fig.4.1).

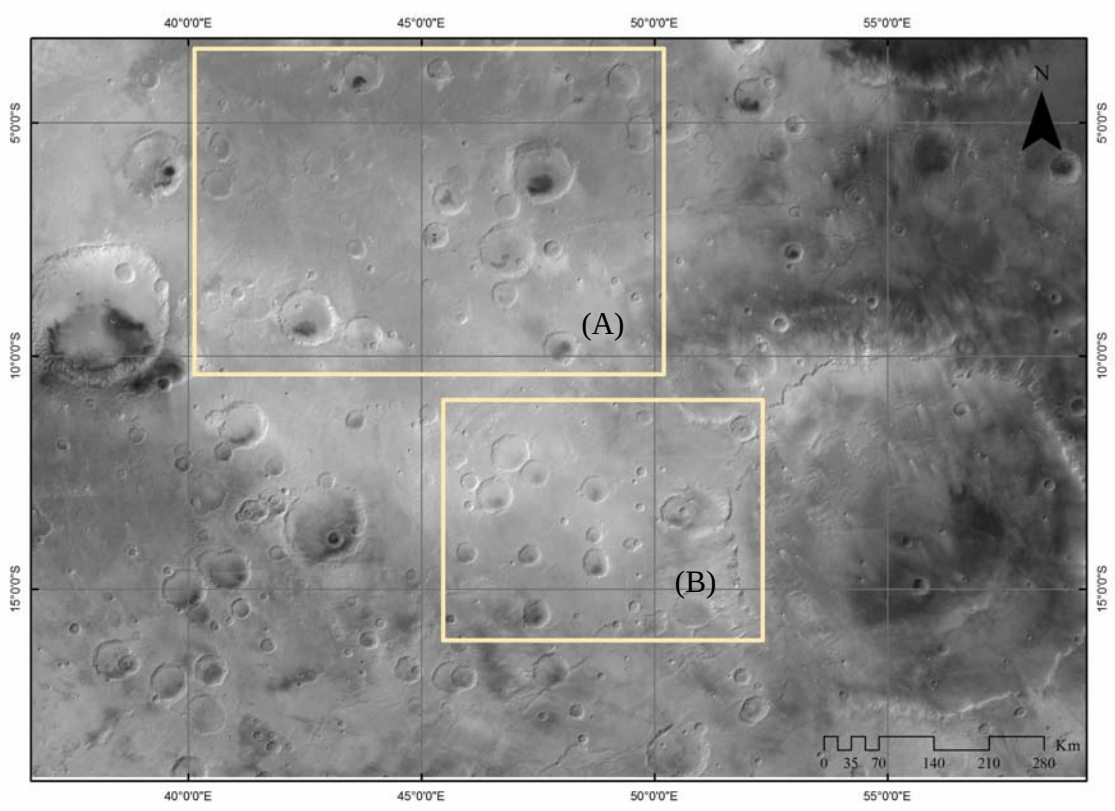


*Fig.4.2. Map showing the broader study area on Mars, and two excerpts (A, B) submitted for CHT and DoH analysis respectively. Image from Mars Orbiter Camera (MOC) of Mars Global Surveyor (source: USGS Planetary GIS Web Server).*

The Planetary GIS Web Server of the United States Geological Survey (USGS) makes available a GIS-ready digital terrain model (DTM) of the Martian surface, released by NASA Goddard Flight Center. The DTM used here was acquired by the Mars Orbiter Laser Altimeter (MOLA) of the Mars Global Surveyor (MGS) robotic spacecraft at a resolution of ~ 463 m/pixel (observed topography within a 0.00781 × 0.00781 degree

window). In addition to the narrow-angle camera image (Fig. 4.2), the DTM (Fig. 4.3.) portrays the qualitative characteristics of the Martian impact craters in the study area.

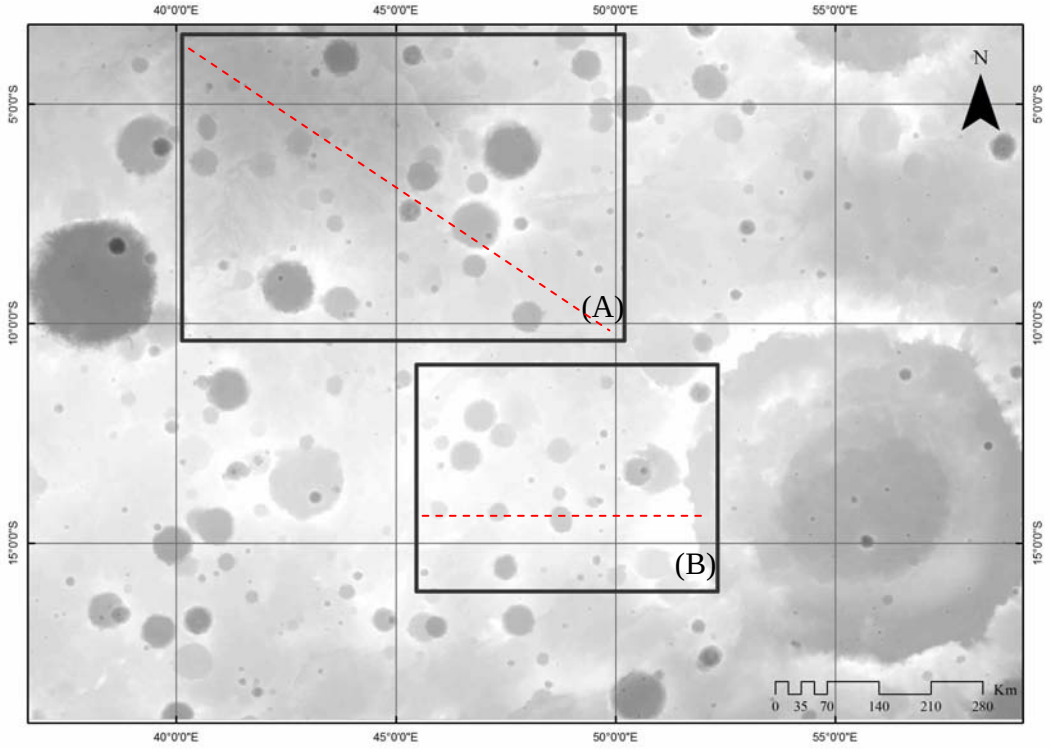


*Fig.4.3. The digital terrain model (DTM) of the study area.*

Impact craters are perceived as negative topographic features in relation to their immediate neighborhood. Contrary to concavities of different origin, such as tectonic grabens (chasmata) or erosional channels, impact craters are enclosed by almost perfectly circular edges. But how do we define crater edges? Landforms are perceived through relief undulations. From the outside inwards, the profile of an impact crater is morphologically expressed by a ridge (resulting from the buckling of the lithosphere during collision) that sharply goes over a low-lying flat area. Because the blurry DTM raster image cannot be readily read as is, the fluctuations of the gradient of the DTM (i.e.

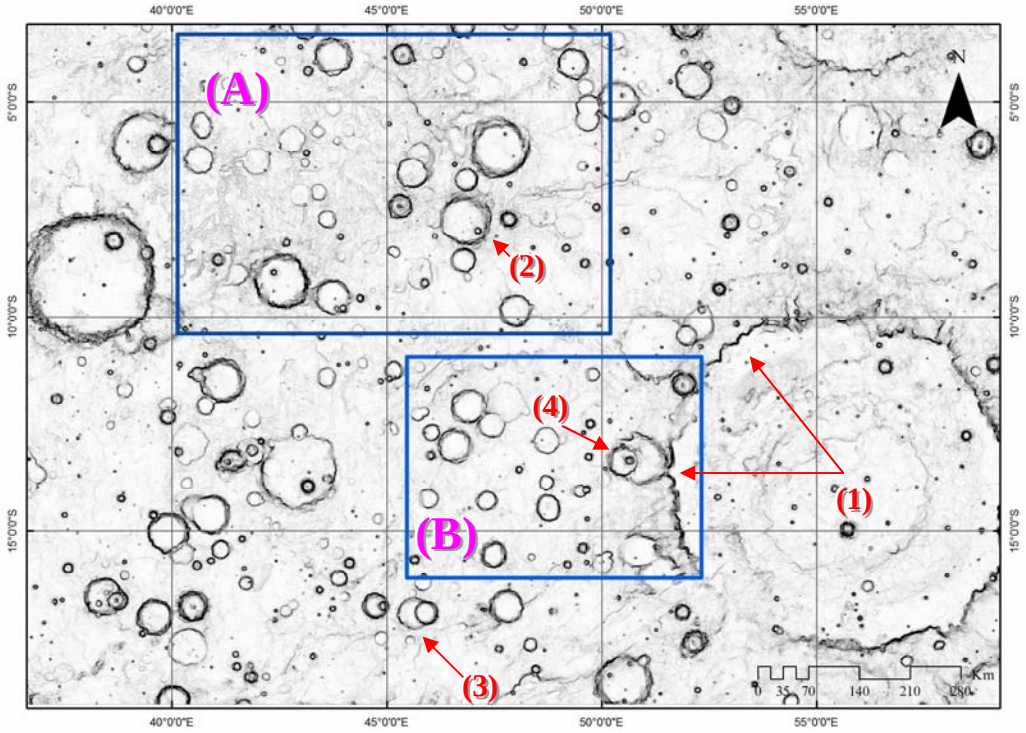


*Fig.4.4. The gradient of the DTM. (1) crater whose circular edge has been eroded acquiring a jigsaw-like shape. (2) crater nesting in crater, (3) overlapping craters, (4) combination of (1), (2) and (3).*

the partial derivative of the relief function) can highlight crater ridges as embossed lines (edges) on a low intensity background (Fig. 4.4). Impact craters range in diameter from ~450 km to as less as 1 km or even lesser. Their perimeter often seems to be partially eroded by the former Martian hydrological cycle (Andrews-Hanna et al., 2007).

Martian impact craters do not exist in isolation but they have been influenced by moderators involving the Martian weather and subsequent meteor showers. As such, crater morphology on Mars is diverse. Aeolian and fluvial processes (Barlow, 2016) may distort the original perimeter of the craters from nearly circular to jigsaw-like edges, as in the case of the prominent crater in the bottom-right corner of Fig. 4.4 (1). In addition,

ongoing bombardment may produce overlapping craters exhibiting complex configurations: from "matryoshka doll"-like structures, where craters are completely nested in larger craters (2 in Fig.4.4), to interlocked rings (3 in Fig.4.4), or a combination of the two (4 in Fig.4.4). Therefore, the apparent complexity of crater shapes encountered on Mars poses a challenge to the methodologies employed here.

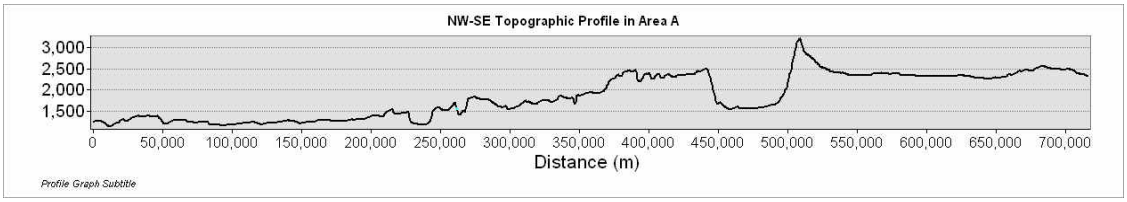


*Fig.4.5 Topography profile of test area A in a NW-SE direction. Topography is characterized by sinusoidal fluctuations while there is an overall increase of the intensity towards the SE.*

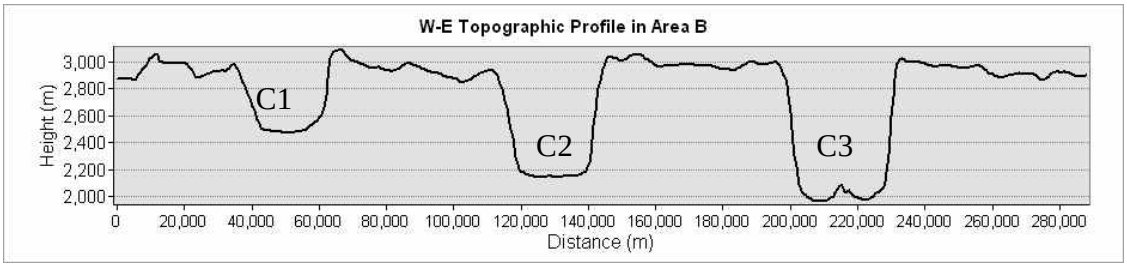


*Fig.4.6. Topography profile of test area B in a W-E direction, drawn across the middle of*

Despite the recurrent morphological pattern in the horizontal sense, Martian topography is anything but monotonous when seen three-dimensionally. Figures 4.5 and 4.6 illustrate two topographic profiles corresponding to the dashed lines in sections A and B respectively (in Fig.4.3) and reveal that meteor craters may crop up at diverse landscapes from tilted sinusoid-like (Fig.4.5) to remarkably flat areas (4.6). Even though the topographic fluctuations should not affect the behavior of CHT, which basically draws votes from a 2D landscape, they might however affect the performance of DoH that relies

on the topographic gradient. CHT and DoH was tested against two distinctive landscape settings designated as A and B in Fig.4.2 in order to compare their performance for both oscillating (A) and plane (B) topographies.

## 5. Results

### *5.1. Circular Hough Transform*

Before applying CHT to image excerpt "A" it is necessary that all feature edges be reduced to single-pixel wide curves (Kim et al., 2005; Stepinski et al., 2006; Bue and Stepinski, 2007). First, a Gaussian kernel 9×9 ($\sigma$=1) was convolved with the image to reduce the noise.

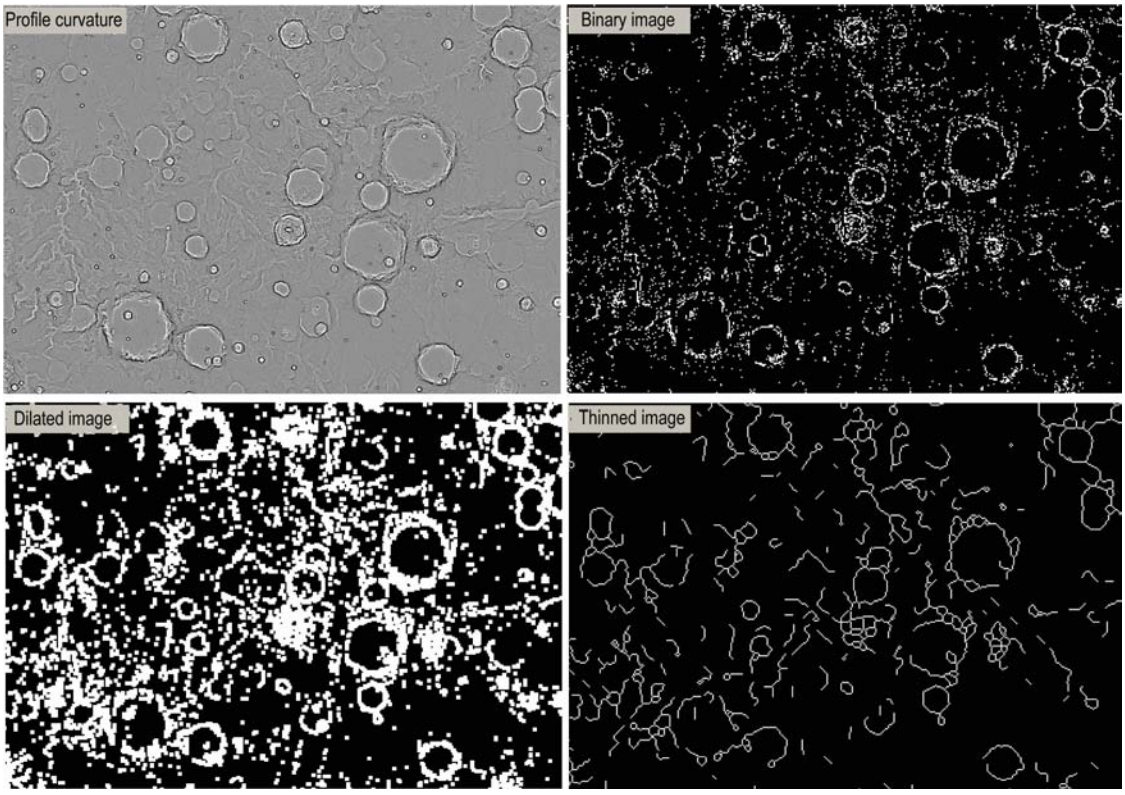


*Fig.5.1. Intermediate processing steps of the Martian DTM leading to a derived image ready for CHT. Top left: profile curvature, top right: binary image, bottom left dilated image, bottom right: thinning of the eroded image after dilation.*

Then the profile curvature was calculated as an indicator of the crater edges. The profile curvature image underwent specific preprocessing steps as suggested by (Bue and Stepinsky, 2007) which included 1) thresholding to create a binary image, 2) a single

morphological closing (dilation and erosion using 3×3 structural elements), and finally thinning using 3×3 structural elements (Bue and Stepinsky, 2007).

Image thresholding is used as a preliminary form of image segmentation. In its simplest form thresholding replaces each pixel in the image by a white pixel, if the pixel's intensity is greater that the threshold or by a black pixel, if the intensity value assigned to that pixel is lower than the threshold.

Morphological closing involves dilation of the image by a structural element, and then erosion of the image by the same element. Dilation aims at expanding (dilating) the boundaries of objects (white pixels) in the binary image by filling (fully or partially) the small voids appearing between the image objects. Then, erosion is the mathematically inverse procedure and involves convolution with a structural element such that the resulting objects in the image appear contracted. Morphological closing thus achieves to fill gaps in imperfect objects while maintaining them contracted. Thinning, on the other hand, is a morphological operator marking out object edges by reducing all linear features to single-pixel thick lines. Tools embedded in commercial geographic information systems (ArcGIS) offer the options for automatic calculation of the above-mentioned image products.

Fig.5.1. illustrates the intermediate image processing steps leading to the thinned image ready for CHT analysis. CHT was performed on the thinned image utilizing the

*CircularHough_Grd* algorithm written for Matlab. The algorithm's parameters read as follows:

*[accum, cirrad] = CircularHough_Grd(img, radrange)*

where i) *accum* creates the accumulator array to receive votes from the CHT, and it should have the same dimensions as the image, ii) *cirrad* creates a column vector with a one-to-one correspondence to the output *circen*, iii) *img* is the image to be processed, iv) *radrange* is the minimum and maximum radii of the circles to be searched.

Having inserted a range of radii (*radragne*) between [2,40] *CircularHough_Grd* returned the accumulation matrix (Fig. 5.2) and the detected circles (Fig. 5.3b). The range of radii was selected in such a way that it captures all of the potential crater sizes appearing in the image. However, as seen from Fig.5.2a, the 2D accumulation array is noisy, and the neighborhoods of candidate crater centers are broad and overlapping, marked by the continuous bright green coloring. This sort of distribution yields a similarly noisy 3D accumulation array with poor signal-to-noise rations (contrary to prominent peaks in the paradigms in Fig.3.10 that where they can be associated with circle centers confidently). *CircularHough_Grd*, therefore, allocates candidate centers in image areas that are hardly relevant to crater centers (Fig. 5.3b). This obviously owes to the noisy character of the pre-processed image (Fig. 5.3a). The procedure was repeated on area B which is characterized by a flatter topography.

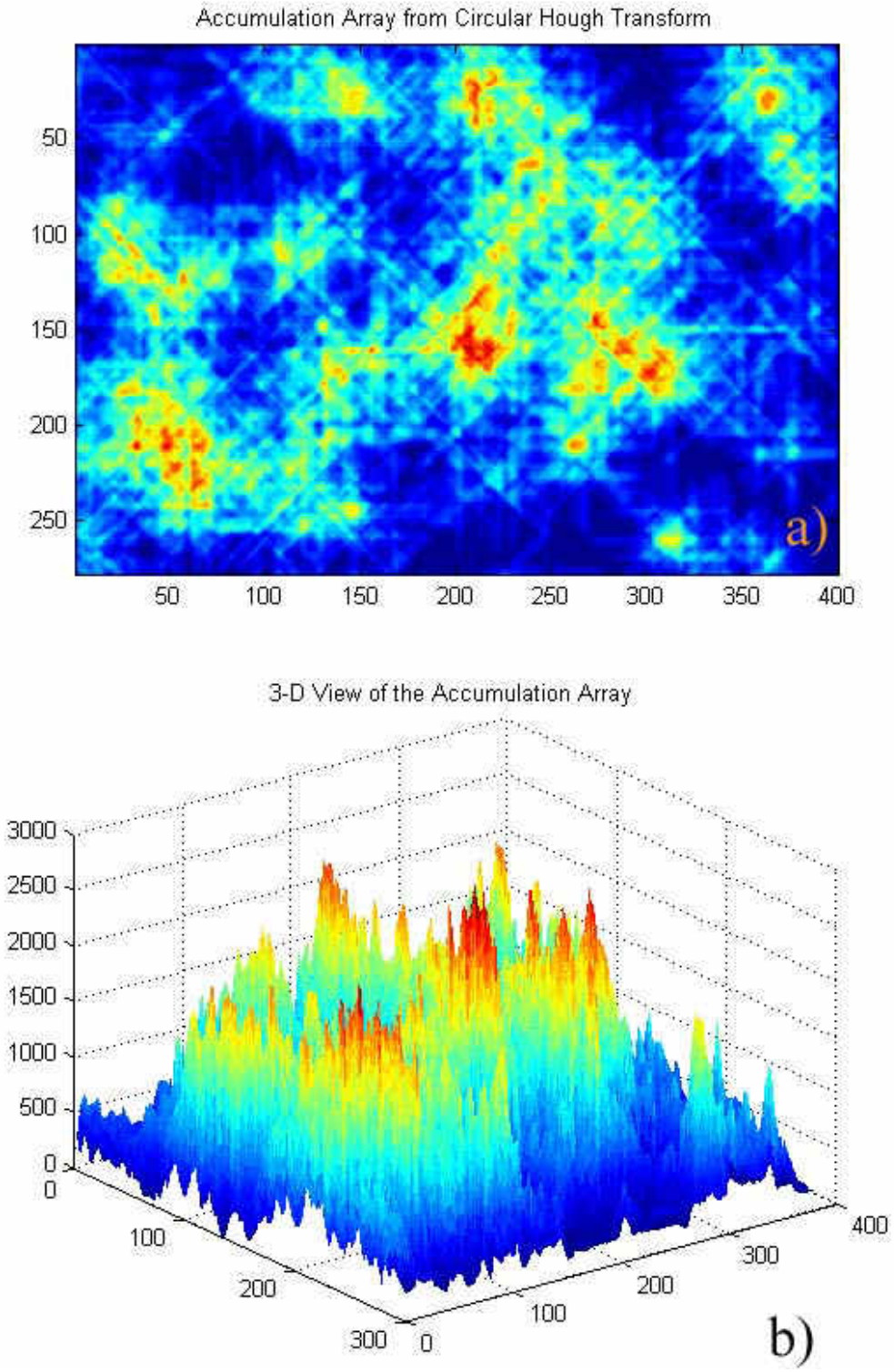


*Fig.5.2. a) Accumulation matrix, provided as raster, for area A. Casting of votes appears to be spread across the accumulation matrix rather than explicitly focalized. b) 3D representation of the accumulation matrix. Note the absence of prominent peaks.*

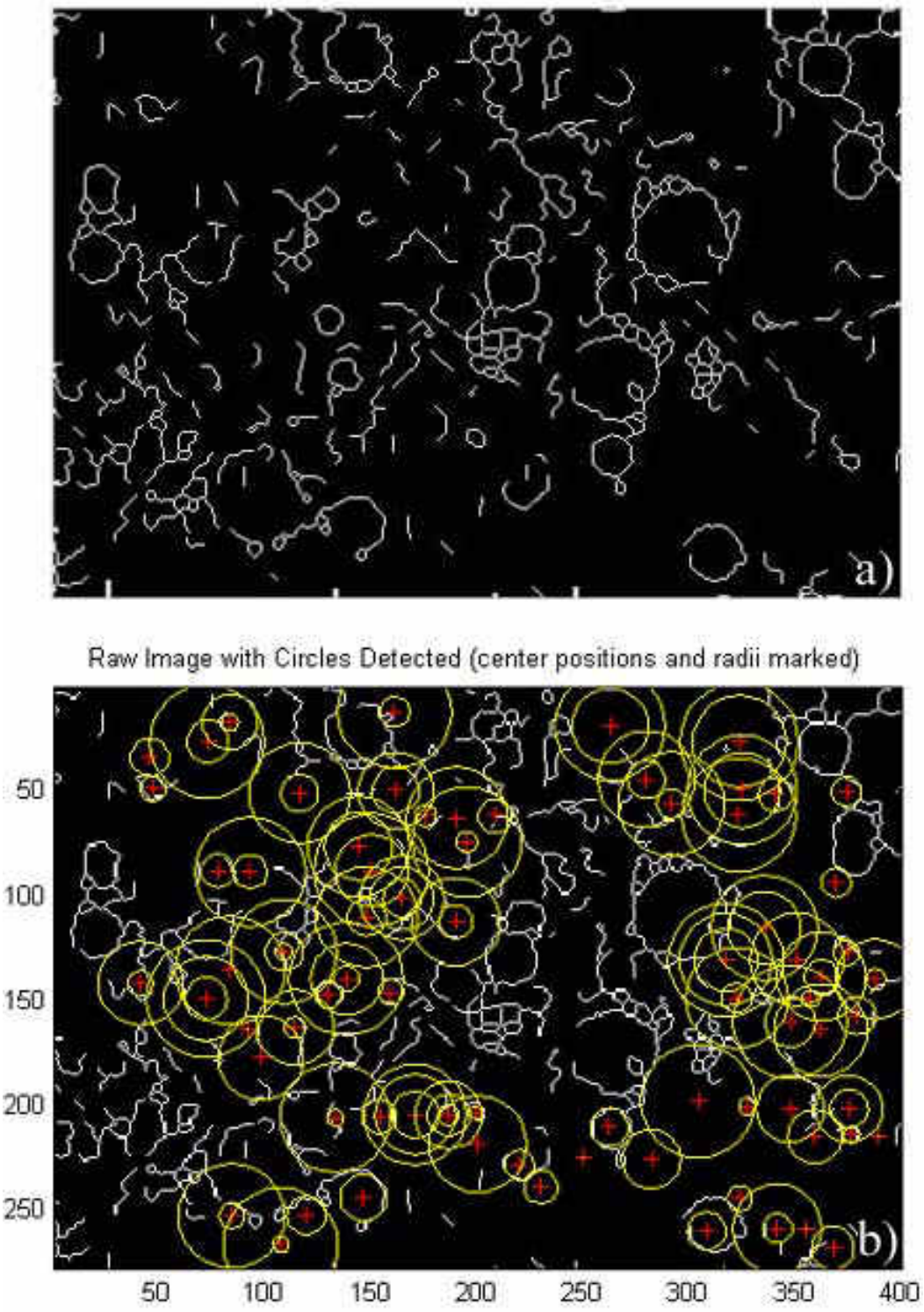


*Fig.5.3. Area A: a) derived image after morphological closing and thining of the curvature of the Martian DTM. b) Candidate centers (red crosses) and circle perimeters generated by the CircularHough_Grd algorithm.*

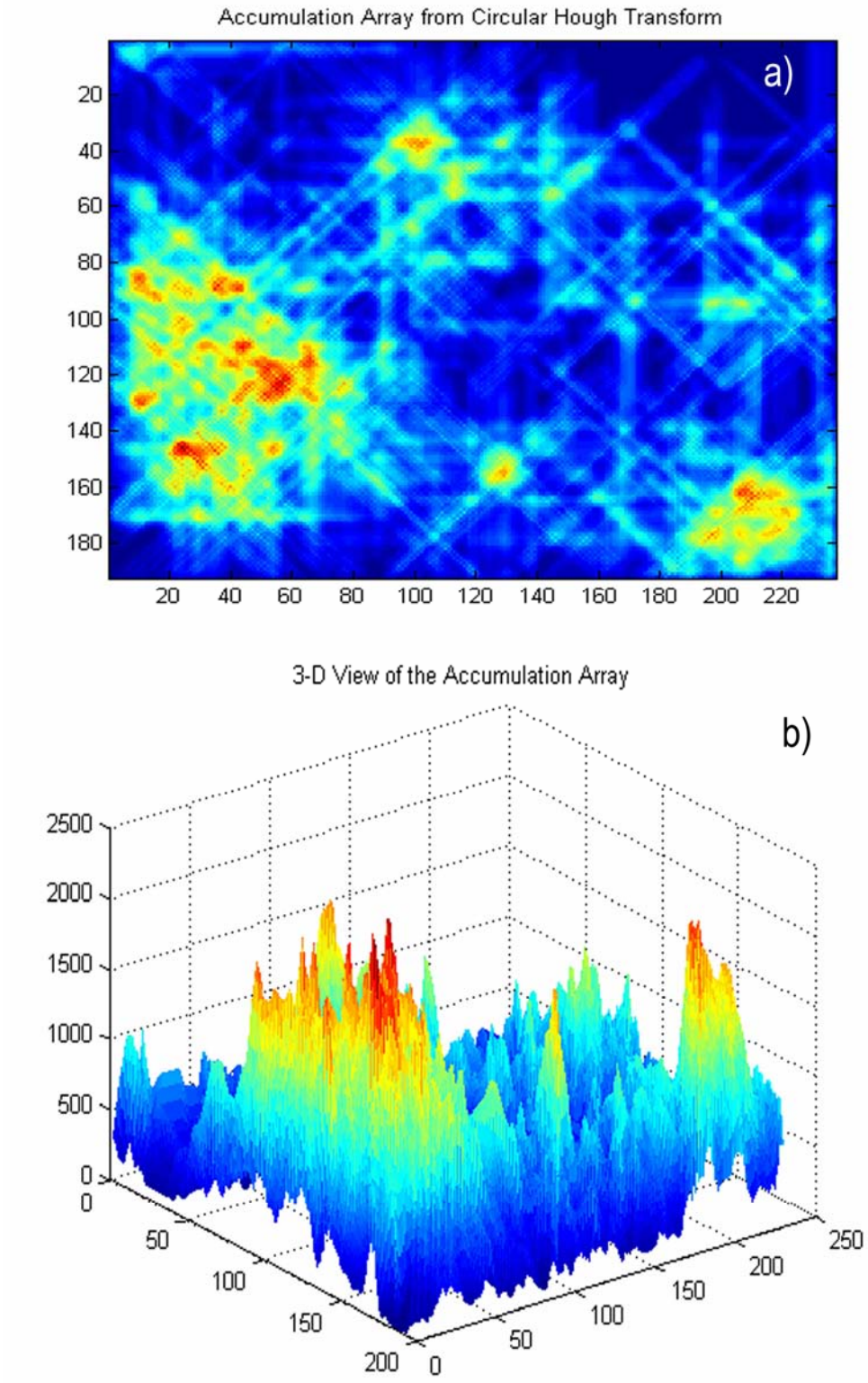


*Fig.5.4. a) Accumulation matrix provided as raster for area B. b) 3D representation of the accumulation matrix.*

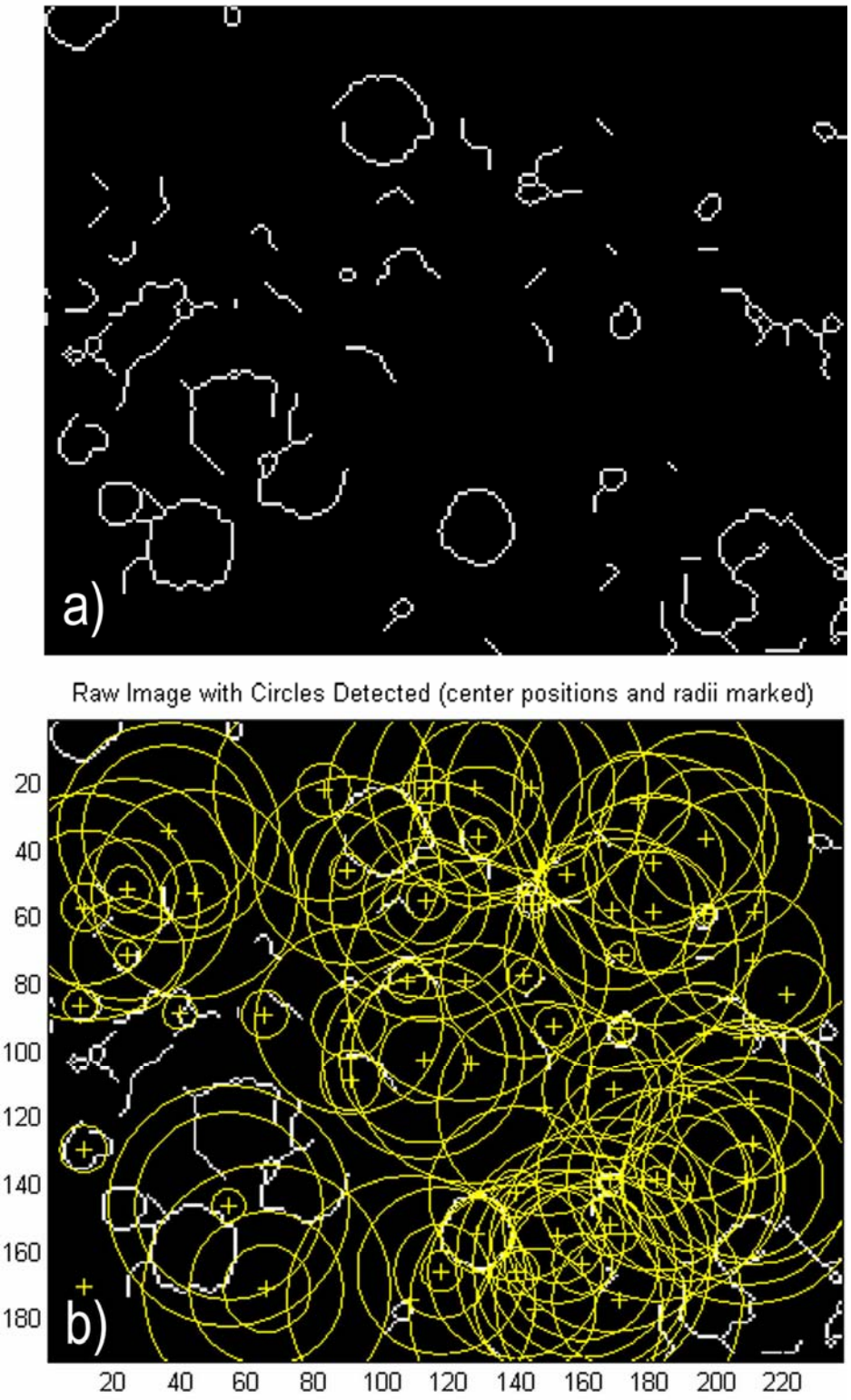


*Fig.5.5. Area b: a) derived image after morphological closing and thinning of the curvature of the Martian DTM b) Candidate centers (yellow crosses) and circle perimeters generated by the CircularHough_Grd algorithm.*

The results of CHT for area B (Fig. 5.4, 5.5) do not score better for area B, implying that subdued topographic oscillations do not necessarily improve the performance of CHT.

*5.2. Blob detection*

For the detection of impact craters as blobs, this study takes advantage of the *blob_doh* algorithm available from the *scikit-image* library for image processing in Python programming language. The algorithm defines the center of a blob where the Hessian is maximized, and then delivers their (*x*,*y*) coordinates and the standard deviation of the Gaussian kernels convolved with the Hessian matrix. The radii of the blobs are approximately equal to the standard deviation of the Gaussian kernel. One shortcoming of *blob_doh* is that it cannot detect radii smaller than 3 pixels wide due to the box filters (Bay et al., 2008) employed in the approximation of the Hessian Determinant. The syntax of *blob_doh* in *python* is as follows:

*blob_doh (image, min_sigma=a, max_sigma=b, threshold=c)*

whereas *image* is the image to be analyzed, *min_sigma* and *max_sigma* (a and b, scalars) the minimum and maximum standard deviations of the Gaussian kernel for detecting small and large blobs respectively and *threshold* (c, scalar) is known as the *scale parameter* that defines the smallest scale-space maxima to be detected.

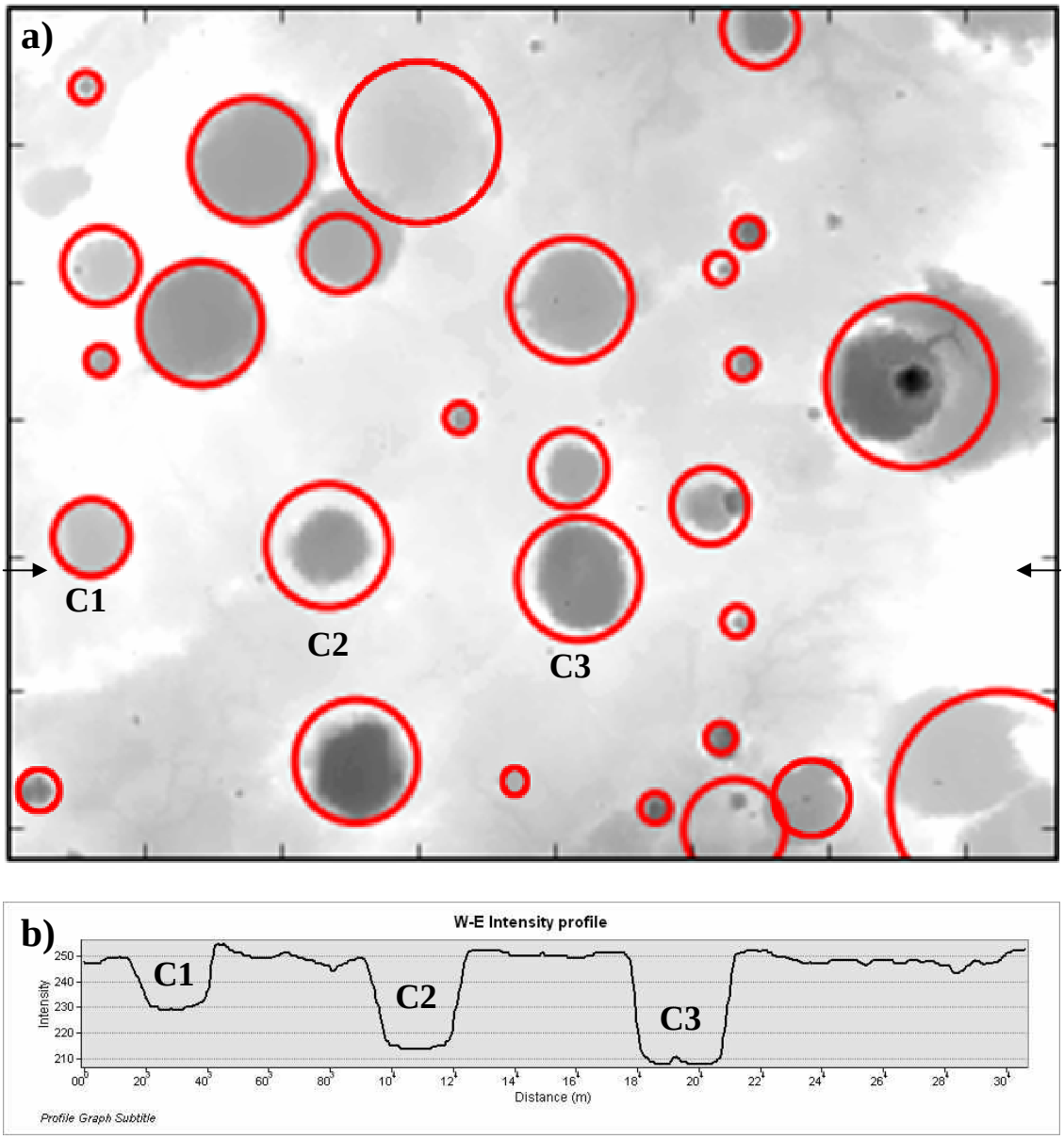


*Fig. 5.6. a) Test area B (outlined in the DTM presented in Fig.14). Red circles correspond to blobs detected by blob_doh function. Detection parameters: [80, 3, 0.001]. Small arrows indicate the direction of the intensity profile. b) Intensity profile of test area B in a NW-SE direction. Dramatic depressions (C1, C2, C3) correspond to impact craters.*

Generally, it is recommended that blob detectors operate on grayscale images. Their performance will be challenged in color images, as the summation of the derivatives of the individual channels will eliminate any correlation between the color channels if the

derivatives trend in opposite directions (Ming and Ma, 2007). The DTM used here is in grayscale mode anyway.

Fig. 5.6a corresponds to test area B excerpted from the broader DTM image (Fig. 4.2). Before applying the *blob_doh* algorithm the image underwent noise reduction by convolving it with a 9×9 Gaussian kernel. A standard deviation $\sigma$=1 was chosen as it lends a greater smoothing effect to the kernel than a smaller one. Fig.5.6b illustrates the representative intensity profile of the image in W-E direction. Generally, the intensity landscape corresponds to a relatively horizontal plane, intermittently perforated by abrupt depressions that reflect impact craters. Experiments with a series of combinations of *min_sigma, max_sigma* and *threshold* returned optimum results for the triplet [80, 3, 0.001], for which *blob_doh* detected 28 out of 32 craters implying 88% of success, which is a remarkably good performance.

The performance of *blob_doh* was further challenged by testing it against the more complex landscape of section "A" (Fig. 4.3), which is characterized by sinuous-like topographic fluctuations on an inclined plane. From Fig. 5.7 it becomes apparent that *blob_doh* captures a great portion of the craters existing in the image represented by darker areas (true craters) but also encircles bright areas which do not correspond to craters (false craters). By default, DoH operator searches for local extrema between 0-255 in the intensity landscape corresponding to either topographic maxima or minima. Area B is typified by topographic minima only and for this reason it is free of circles associated to convex landforms. However, this is not the case for test area A where topographical

hillocks occasionally interpose in the crater-perforated landscape. Because of this, *blob_doh* will inevitably encircle both concave (dark blobs) and convex (bright blobs) landforms; the latter are unwanted.

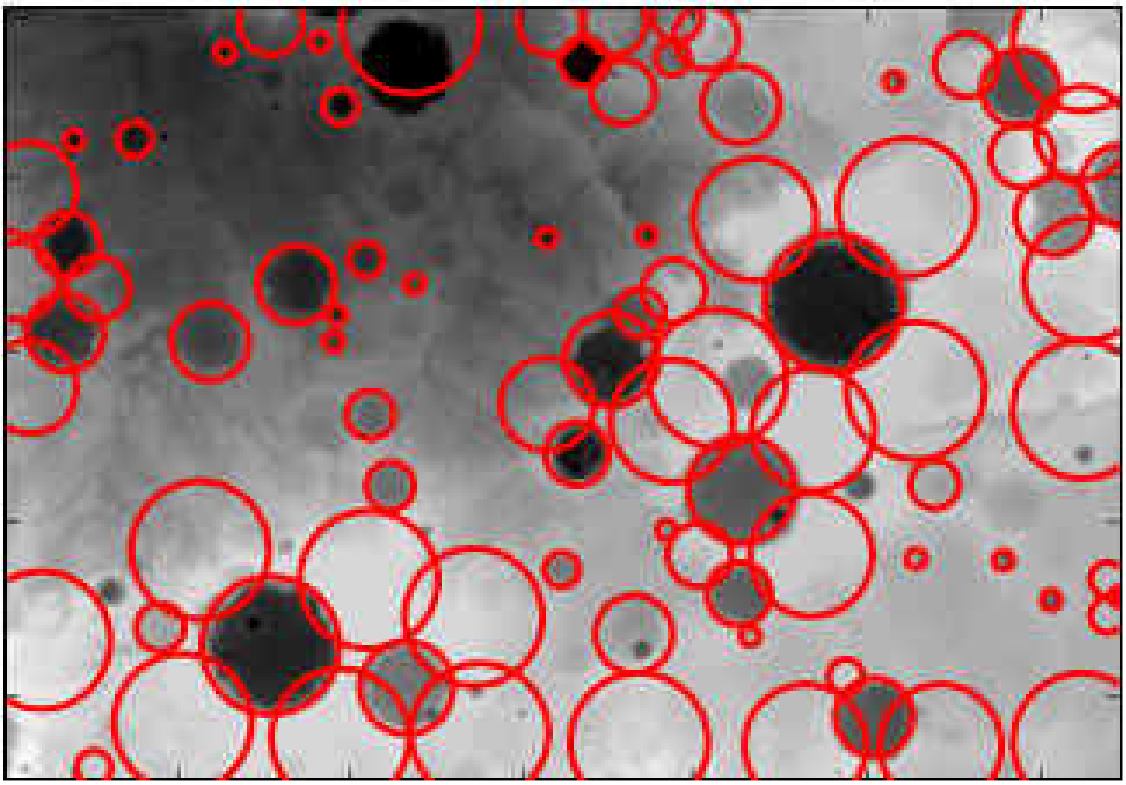

*Fig. 5.7. Output of the blob_doh function after analyzing the excerpt from the Martian DTM (test area A). Red circles correspond to blobs detected by blob_doh, being either convex or concave. Detection parameters: [80, 3, 0.001]*

One way to get rid of false craters is to insert an intensity cut-off in the Python so that *blob_doh* is prevented from circling around bright blobs. By progressively lowering the cut-off we managed to free the output from false craters only when an intensity value of 80 was reached. Nevertheless, in doing so, *blob_doh* captures a smaller number of true craters (29 out of true 60), excluding craters outcropping in bright areas (i.e. high elevations) as seen from Fig. 5.8a. This can be straightforwardly explained by recalling the shape of the profile of the intensity landscape (Fig. 5.8b). Insertion of an intensity cut-

off at value 80 (Y-axis) inevitably leads to the rejection of almost half of the image area and exclusion of craters resting at higher elevations.

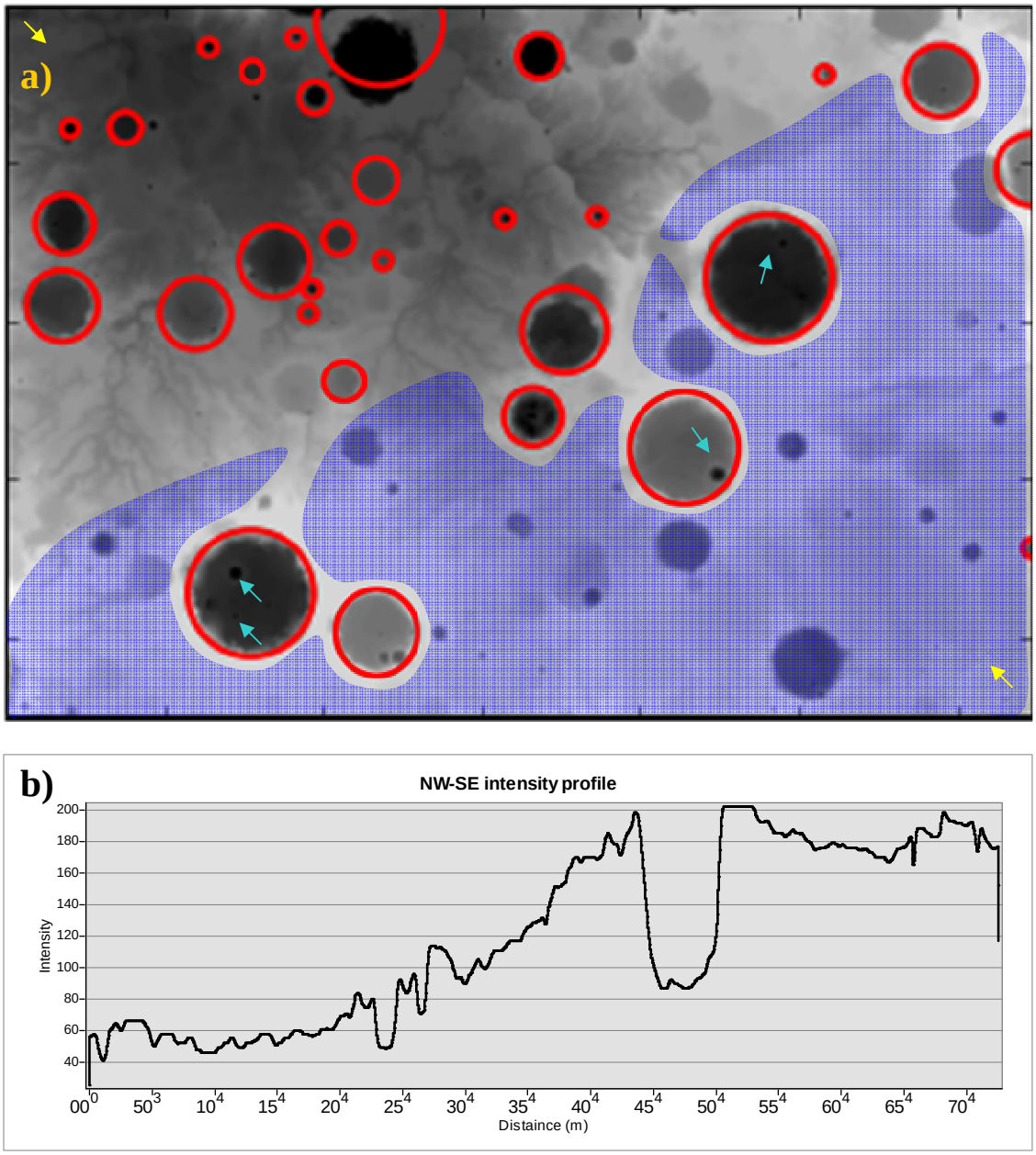


*Fig.5.8. a) Blob detection on test area B after inserting an intensity cut-off at 80. Detection parameters: [80, 3, 0.001]. Blue-shaded area indicates the portion of image abolished by inserting the intensity cut-off. Yellow arrows indicate the direction of the intensity profile. Bright-green arrows point at craters nested within larger craters. b) Intensity profile of test area B in a NW-SE direction. Topography is characterized by sinusoidal fluctuations while there is an overall increase in intensity towards the SE.*

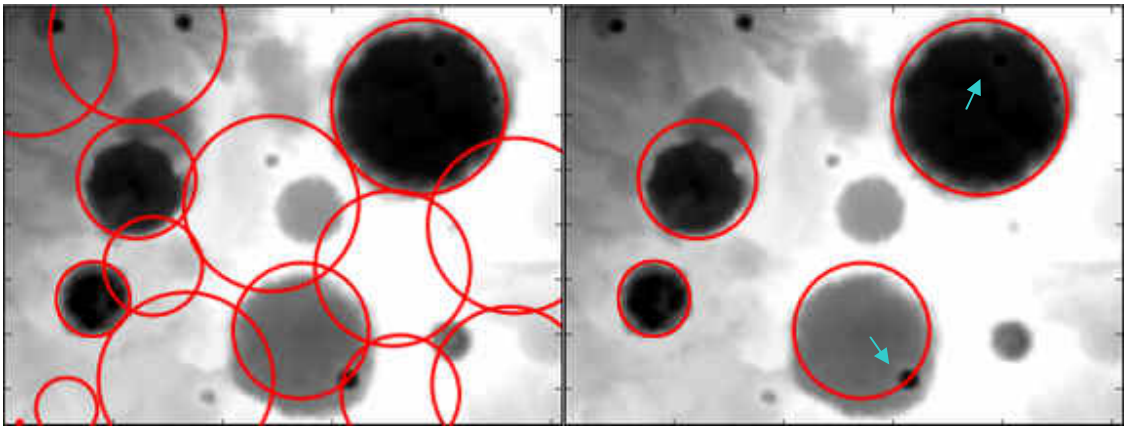

*Fig.5.9. Blob detection at a greater scale before (left) and after (right) applying the intensity cut-off at value 80. Detection parameters: [80, 3, 0.001]. Bright-green arrows point at craters emplaced within larger craters.*

Apart from testing DoH's sensitivity to diverse topographies, we also test its sensitivity as to the scale of observation. A closer look at Fig. 5.9 reveals that a few craters may exhibit internal structure, meaning smaller craters that were emplaced within larger craters. At the scale of Fig 5.9 *blob_doh* treats such craters as uniform structures eliminating any information for their interior. Fig. 5.9 (coming central-right sector of Fig. 5.8a) illustrates an excerpt from Fig. 5.8a at greater scale. Application of *blob_doh* (using the detection parameters and intensity cut-off value as in Fig.5.9) returns blobs that still maintain their internal structure disclosed.

Analysis goes further by turning the scale of observation on an example involving a single crater only (Fig. 5.10). At this scale of observation the internal structure of the crater becomes more explicit revealing smaller but still sizable craters for the given observation scale. Despite the elimination of false blobs resulting from the brighter surrounding using an intensity cut-off value of 30 (Fig. 5.10), *blob_doh* keeps suppressing the internal structure of the crater.

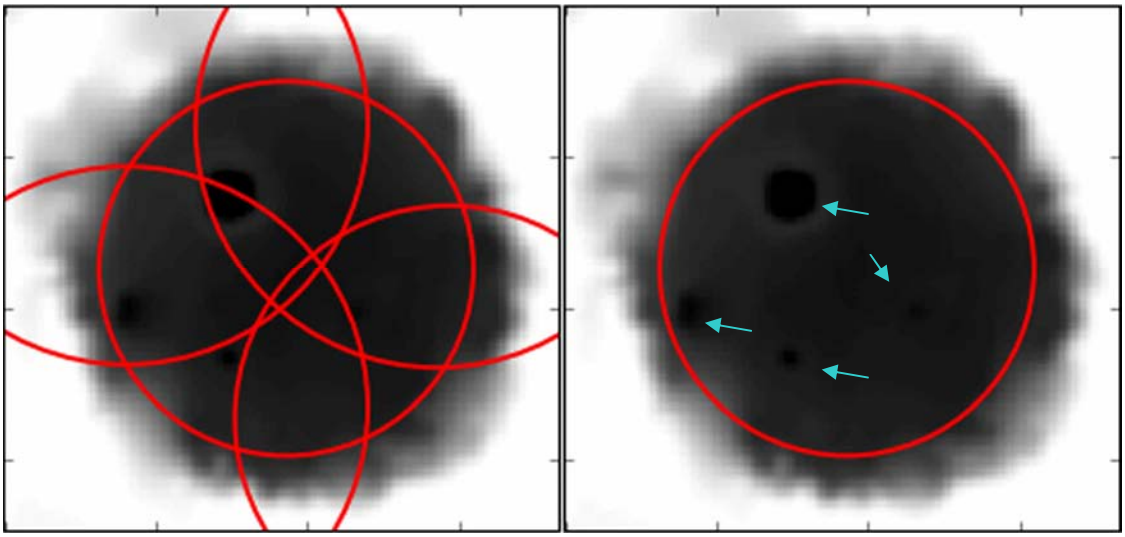

*Fig. 5.10. Blob detection at the scale of a single crater before (left) and after (right) applying the intensity cut-off at value 30. Detection parameters: [80, 3, 0.001]. Bright-green arrows point at craters exhumed*

## 6. Discussion

Circular Hough Transform was run on the Martian DTM and returned a blurry accumulation matrix, lacking prominent peaks as strong candidates for crater centers (Fig. 5.2- 5.5). CHT results turned out to be poor, failing to capture a meaningful number of craters. This deficiency is attributed to 1) the imperfect instantiation of the craters in the skeletonized image due to natural erosion of the crater edges, 2) low signal-to-noise ratios as edges from other irrelevant objects (i.e. relict drainage network and other types of topographic discontinuities) have permeated into the skeletonized image, casting false votes in the accumulation matrix.

Investigators on the CHT detection of impact craters (Kim et al., 2005; Bue and Stepinksi, 2007) address the deficiency of CHT to detect impact craters directly from the skeletonized image. Bue and Stepinski (2007) managed to enhance the detection capacities of CHT by employing a long-drawn-out process (which lies beyond the purposes of this work) deploying algorithms which fragment the DTM into numerous small images, each aimed at wrapping one crater exactly. In this way the noisy influence of other objects lying in the neighborhood of a crater is waned.

On the other hand, the *blob_doh* algorithm yielded noteworthy success when applied to sets of craters cropping up on a horizontal plane, returning a success rate of 88%. Among the detected craters are included craters of all sizes, even the less prominent ones in terms of contrast. This score is better than that achieved by CHT.

Nevertheless, the fact that some craters emplaced in bigger craters may escape *blob_doh* scrutiny may not be perceived as failure for the current state-of-the-art of computer vision. For instance, craters exhumed in other craters will too go amiss when the image is "flooded" during the widely applicable watershed segmentation procedure. And watershed segmentation has been the workhorse of image processing for 30 years; there is no need to apologize for it.

In spite of the notable success of *blob_doh* in the first example, such high rates of success are not universal. The performance of *blob_doh* on a topographically more complex excerpt of the Martian DTM, demonstrating inclination and sinusoidal topographical variability, scored poorer, yielding a success rate of 30%. Sinusoidal topography necessitated the introduction of an intensity cut-off value in order to prevent hill-like blobs from being revealed.

However, introduction of the cut-off will inevitably discard all image "elevations" above that which, for the case of the DTM excerpt illustrated in Fig.5.8, correspond to a large portion of the image area. This image information will inevitably be lost, as well as any craters emplaced in high-lying areas. Such a deficiency instantly narrows the range of DTMs suitable for crater detection using *blob_doh* to flat perforated landscapes only. Despite the loss of information induced by the more complex landscape, *blob_doh* scored more true positives than CHT. This primarily owes to the fact that *blob_doh* is less prone to noise than is CHT for the given pre-processed image. Generally, it is more prudent to

detect more conservatively and fail to spot a few craters rather than turn up with many false responses.

## 7. Conclusions and future directions

Expectations for the conventional CHT to detect efficiently meteorite craters on the Martian digital terrain model are low as long as the processed image cannot be substantially released from noise introduced by the presence of surrounding features (e.g. relict drainage network, rims of irregular basins etc). Adaptations of CHT that make use of meticulously pre-processed images including fragmentation of the image into small icons (Bue and Stepinski, 2007) have been characterized by a higher rate of success. Nevertheless, the higher computational cost involved in such an approach (Bue and Stepinski, 2007) renders the adapted CHT less practical for routine crater detection. Nevertheless, employment of the anisotropic diffusion technique at the pre-processing stage might be capable of returning images with subdued noise without weakening much the objects of interest (Karantzalos, 2004). Anisotropic diffusion generates a family of parameterized images with each subsequent image being the simplification of its immediate predecessor by solving the diffusion equation and convolving a Gaussian kernel (Perona and Malik, 1990).

On the other hand, *blob_doh* succeeded in capturing the vast majority of the craters cropping up in a flat Martian terrain. The success rate declined when a more complex terrain was encountered. Still *blob_doh* generated a higher success rate than CHT even if a complex topography was involved. Despite the occasional need for heuristics (i.e. selection of an intensity cut-off deliberately), it is thought that *blob_doh* can outperform CHT in routine crater detection because (1) *blob_doh* can cope with the image noise

better than CHT and (2) image preprocessing requirements are least: it can be directly applied to the DTM or, optionally, after some Gaussian smoothing.

Future work will be dedicated to tackling the shortfalls caused by the insertion of an intensity cut-off in landscapes shown overall topographic inclination. One way to go around the problem would be to divide the image into apparent windows where the individual topographies can be practically considered horizontal, so that the insertion of an intensity cut-off excludes topographic bulges without affecting the delineation of the craters. Such an improvement would expedite impact crater detection on the rocky planets and facilitate astronomical research in the Solar System.

## 8. References

Andrews-Hanna, J.C., R.J. Phillips, and M.T. Zuber. 2007. Meridiani Planum and the global hydrology of Mars. *Nature*, 446, 163-166.

Argialas, D., and S. Krishnamoorthy, (1992). Detection of lines and circles in maps and engineering drawings. In Fritz and Lucas (Eds) International Archives of Photogrammetry and Remote Sensing, Vol. XXIX, part B, Commision III, pp.392-399.

Barlow, N.G. 1988. Crater Size-Frequency Distributions and a Revised Martian Relative Chronology. *Icarus*, 75, 285–305.

Barlow, N. G. *Stones, wind and ice.* Lunar and Planetary Institute. Retrieved 2016-03-19 (http://www.lpi.usra.edu/publications/slidesets/stones/).

Barraud, J. 2006. The use of watershed segmentation and GIS software for textural analysis of thin sections. *Journal of Volcanology and Geothermal Research*, 154, 17–33.

Bay, H., Ess, A., Tuytelaars, T., van Gool, L. 2008. Speeded-up robust features (SURF). *Computer vision and image understanding*, 110, 346-359.

Bayer, U. 1985. Pattern recognition problems in geology and paleontology. *Springer-Verlag*, 229p.

Berman, D.C., D.A. Crown, and L.F. Bleamaster III. 2009. Degradation of mid-latitude craters on Mars, *Icarus*, 200, 77-95.

Beucher, S. and Lantuéjoul, C. 1979. Use of watersheds in contour detection. In International workshop on image processing, real-time edge and motion detection, September 17-21, Rennes, France.

Brunetti, T., Guzzetti, F., Cardinali, M., Fiorucci, F., Santangelo,M., Mancinelli, P., Komatsu, G., Borselli, L. 2014. Analysis of a new geomorphological inventory Of landslides inValles Marineris, Mars. *Earth and Planetary Science Letters*, 405, 156–168.

Bue, B.D. and Stepinski, T.F. 2007. Machine Detection of Martian Impact Craters From Digital Topography. IEEE Transactions on Geoscience and Remote Sensing, 45, 265-274.

Carr, M.H., Head, J.W. 2010. Geologic History of Mars. *Earth Planet. Sci. Lett*, 294, 185–203.

Claeys, P., Morbidelli, A. 2011. Late Heavy Bombardment. In: Gargaud et al. (Eds). Encyclopedia of Astrobiology, pp. 909-991.

Duda, R.O. and Hart, P.E. 1972. Use of the Hough transform to detect lines and curves in pictures. *Graphics and image processing*, 15, 11-15.

Gomes, R., Levison, H. F., Tsiganis, K., Morbidelli, A. 2005. Origin of the cataclysmic Late Heavy Bombardment period of the terrestrial planets. *Nature*, 435, 466–469.

Grauman, K., Leibe, B. 2011. *Visual object recognition*. Morgan & Claypool, pp. 163.

Grauman, K. 2014. Fitting: Voting and the Hough Transform. Retrieved on 2015-12-03 (http://www.cs.utexas.edu/~grauman/courses/spring2011/slides/lecture8_hough.pptx)

Hartmann, W. K., Neukum, G. 2001. "Cratering Chronology and Evolution of Mars". In Kallenbach, R. et al. (Eds) Chronology and Evolution of Mars. Space Science Reviews, 12, pp. 105–164.

Illingworth, J. and Kittler, J. 1987. The adaptive Hough transform. *IEEE Trans. Pattern Anal. Mach. Intell.*, 9, 690-698.

Karantzalos, K. G. and Argialas, D. P. 2004. Towards automatic olive tree extraction from satellite imagery. Geo-Imagery Bridging Continents. XXth ISPRS Congress, pp.12-23.

Karantzalos, K.G. 2004. Combining anisotropic diffusion and alternating sequential filtering for satellite image enhancement and smoothing. *Remote Sensing*, 5238, 461-468

Kaspers, A. 2011. *Blob Detection*. Biomedical Image Sciences, Image Sciences Institute, UMC Utrecht. Retrieved on 2015-11-04 (https://www.google.gr/url?sa=t&rct=j&q=&esrc=s&source=web&cd=1&cad=rja&uact=8&ved=0ahUKEwijtC1oNbLAhXKbBoKHdBEDE4QFggaMAA&url=http%3A%2F%2Fdspace.library.uu.nl%2Fbitstream%2Fhandle%2F1874%2F204781%2FBlob%2520detection%2520Final%2520version.pdf%3Fsequence%3D1&usg=AFQjCNGtWbu2BPT0LRc4StA89H699h8jLg&sig2=PuLXaYc4Ma_PkmZ-BQO0Hg&bvm=bv.117218890,d.d2s.)

Kim, J., R., Muller, J.-P., van Gasselt, S., Morley, J, G., Neukum, G., and the HRSC CoI Team. 2005. Automated Crater Detection, A New Tool for Mars Cartography and Chronology. *Photogrammetric Engineering & Remote Sensing*, 71, 1205–1217.

Koenderink, J.J. 1984. The structure of images. *Biological Cybernetics*, 50, pp. 363–370.

Li, G., Liu, T., Nie, J., Guo, L., Malicki, J. Mara, A, Holley, S.A., Xia, W., Wong, S.T. 2007. Detection of blob objects in microscopic zebrafish images based on gradient vector diffusion. *Cytometry A*, 71, 835-845.

Lindeberg, T. 1993. Detecting salient blob-like image structures and their scales with a scale-space primal sketch: a method for focus-of-attention. *International Journal of Computer Vision*, 11, 283-318.

Lindeberg, T. 1998. Feature detection with automatic scale selection. *International Journal of Computer Vision*, 30, 79-116.

Mikolajczyk, K. and Schmid, C. 2004. Scale and affine invariant interest point detectors. *International Journal of Computer Vision*, 60, 63-86.

Ming, A., Ma, H. 2007. A blob detector in color images. *6th ACM international conference on Image and video retrieval Proc*., pp. 364–370, January 2007

Mingzhu, Z., and Huanrong, C. 2008. A new method of circle's center and radius detection in Image Processing. *Proceeding of the IEEE International Conference on Automation and Logistics*, pp. 2239-2242.

Narashimhan, S. 2012. Computer Vision. Retrieved on 2016-01-03. http://www.cs.cmu.edu/afs/cs/academic/class/15385-s12/www/lec_slides/lec-1.ppt

Pătrăucean, V., Gurdjos, P., and Grompone von Gioi, R.2012. A Parameterless Line Segment and Elliptical Arc Detector with Enhanced Ellipse Fitting. A. In: Fitzgibbon et al. (Eds.): ECCV 2012, Part II, LNCS 7573, pp. 572–585.

Perona, P. and Malik, J. 1990. Scale-space and edge detection using anisotropic diffusion. *IEEE Transactions on Pattern Analysis and Machine Intelligence*, 12, 629–639

Prakash, J. and Rajesh, K. 2008. Human Face Detection and Segmentation using Eigenvalues of Covariance Matrix, Hough Transform and Raster Scan Algorithms. *International Journal of Computer, Electrical, Automation, Control and Information Engineering*, 2, 707- 715.

Pyle, R. 2012. *Destination Mars*. Prometheus Books. pp. 73–78.

Rhody, H. Lecture 10: Circular Hough Transform. Retrieved on 2015-11-04. (https://www.google.gr/url?sa=t&rct=j&q=&esrc=s&source=web&cd=1&cad=rja&uact=8&ved=0ahUKEwiH9bfm3e_KAhUqz3IKHZMqB38QFggbMAA&url=https%3A%2F%2Fwww.cis.rit.edu%2Fclass%2Fsimg782%2Flectures%2Flecture_10%2Flec782_05_10.pdf&usg=AFQjCNGMEcBDMuBuMpMiVxjhCVegUYG60A)

Stepinski, T.F. Ghosh, S., Vilalta, R. 2006. Automatic recognition of landforms on Mars using terrain segmentation and classification. In N. Lavrač, L. Todorovski, and K.P. Jantke (Eds): DS 2006, LNAI, pp. 255-266.

Verma, P., Dubey, M., Basu, S., Verma, P. 2012. Hough Transform Method for Iris Recognition-A Biometric Approach. *International Journal of Engineering and Innovative Technology*, 1, 43-48.

Witkin, A.P. 1983. Scale-space filtering. In *Proc. 8th Int. Joint Conf. Art. Intell.*, Karlsruhe, West Germany, pp. 1019–1022.

Xiao, Z., Weij, P. 2006. Detection of circle based on Hough transform. 2006. *Transducer and Micro System Technologies*, 8, 25-34.

Zhong, L., Zhang, J.-M., Zhao, X., Tan, R.S., Wan, M. 2014. Automatic Localization of the Left Ventricle from Cardiac Cine Magnetic Resonance Imaging: A New Spectrum-Based Computer-Aided Tool. *PLoS ONE*, 9, e92382. doi:10.1371/journal.pone.0092382